

Deng, K., Wittmann, H., Hsieh, M.-L., Yang, S.,
von Blanckenburg, F. (2021): Deposition and
retention of meteoric ^{10}Be in Holocene Taiwan
river terraces. - Quaternary Science Reviews,
265, 107048.

<https://doi.org/10.1016/j.quascirev.2021.107048>

Deposition and retention of meteoric ^{10}Be in Holocene Taiwan river terraces

Kai Deng^{a,b}, Hella Wittmann^a, Meng-Long Hsieh^c, Shouye Yang^b, Friedhelm von Blanckenburg^{a,d}

^a *GFZ German Research Centre for Geosciences, Earth Surface Geochemistry, Telegrafenberg, 14473*

Potsdam, Germany

^b *State Key Laboratory of Marine Geology, Tongji University, Shanghai 200092, China*

^c *Department of Earth and Environmental Sciences, National Chung Cheng University, Chiayi, Taiwan*

^d *Institute of Geological Sciences, Freie Universität Berlin, 12249 Berlin, Germany*

**Corresponding author:*

Kai Deng

E-mail: 103459@tongji.edu.cn

Abstract: The cosmogenic meteoric ^{10}Be that is produced in the atmosphere and mainly scavenged by rainfall is a valuable tool for determining dates and rates of Earth surface processes. A key prerequisite for its applications is the knowledge of the long-term ^{10}Be depositional flux to Earth's surface. Previous efforts on obtaining ^{10}Be depositional fluxes include general atmospheric circulation modelling (GCM), empirical fitting of rainfall ^{10}Be records, and determining the inventory of soil profiles of known age. Here, we derive ^{10}Be depositional fluxes from Holocene river terrace ^{10}Be inventories across the Taiwan mountain belt. We measured ^{10}Be and ^9Be concentrations from three terrace profiles, with ^{14}C ages ranging between 3.83 and 9.05 cal. kyr BP and sampling depths of up to 6.2 m.

Based on ^{10}Be inventories of our river terraces, the calculated long-term ^{10}Be depositional fluxes vary from 0.32 to 0.49×10^6 at/cm²/yr in the Taiwan orogen. We identify partial Be retention, surface erosion, multi-phase sediment deposition, and incomplete sampling depth in these terraces as potential causes of flux underestimation. When accounting for each of these factors and their uncertainties, the resulting flux estimates of each terrace show an overlapping range of $0.66\text{--}0.88 \times 10^6$ at/cm²/yr. This newly constrained flux range representative over millennial timescales is thus recommended for Earth surface applications in the fast-eroding Taiwan orogen, especially in regions with similar climatic conditions as the studied terraces. When comparing to flux estimates from other approaches, the flux from the rainfall-based fitting equation exceeds our new terrace-derived flux by more than a factor of two. We consider such high flux to be unlikely for the Taiwan orogen, and suggest that the control of precipitation on the ^{10}Be flux here may be overestimated in rainfall data fitting. The GCM-derived flux overestimates the ^{10}Be depositional flux in this setting to a smaller degree (at least 23%), which is in accordance with findings from previous global data compilation of ^{10}Be fluxes.

Keywords: Holocene, geomorphology, geochronology, Taiwan Island, cosmogenic ^{10}Be , stable Beryllium-9, chemical mobility

1. Introduction

Quantifying dates and rates of Earth surface processes is essential to invoke controls on modern topography and landscape evolution over millennial timescales, with cosmogenic nuclides being one of the most powerful tools (e.g. Bierman et al., 2002; Granger and Schaller, 2014; von Blanckenburg and Willenbring, 2014). In particular, meteoric cosmogenic ^{10}Be with a half-life of 1.39 Myr (Chmeleff et al., 2010; Korschinek et al., 2010) is produced in the atmosphere by cosmic ray spallation (Masarik and Beer, 2009), and is mainly scavenged by rainfall to Earth's surface after adhering to aerosols, and then binds tightly to solid surfaces (Willenbring and von Blanckenburg, 2010). The measured concentration of meteoric ^{10}Be in soil thus relates to its production in the atmosphere, its delivery to the surface, its retention in the substrate, and its stability with regards to erosion (Graly et al., 2011; Willenbring and von Blanckenburg, 2010). As such, meteoric ^{10}Be in soil can be used as a tracer for Earth surface changes over timescales of 10^3 - 10^5 yrs, including determining depositional ages (Egli et al., 2010) and soil residence times (Bacon et al., 2012; Pavich et al., 1986), tracing soil movement (Jungers et al., 2009; Mckean et al., 1993), nutrient uptake by trees (Uhlir et al., 2020), and quantifying rates of erosion and weathering processes over hillslope scales (Jelinski et al., 2019; Johnson et al., 2014; Maher and von Blanckenburg, 2016).

Different from its sister nuclide *in situ* ^{10}Be , which is produced inside minerals (mostly quartz for analysis) with well-known physical rules of production and wide-spread production rate calibration data (Lal, 1991), the delivery and retention of meteoric ^{10}Be is not well-constrained. The reasons include spatial and temporal variations in ^{10}Be production (Masarik and Beer, 2009), complex climatic dynamics in the atmosphere (especially precipitation variability) (Graly et al., 2011; Heikkilä et al., 2013b), physical-chemical mobility in soil (Graly et al., 2010; Willenbring and von Blanckenburg, 2010) and few sites of calibration data available.

To this end, previous efforts on determining ^{10}Be depositional fluxes from modelling and observations (from rainfall and soil profiles) have advanced our understanding on ^{10}Be deposition across

diverse spatial and temporal scales. Modelling efforts encompass general circulation models (GCM), including GISS ModelE (Field et al., 2006) and ECHAM5-HAM (Heikkilä et al., 2013a), which are coupled to ^{10}Be production functions (Kovaltsov and Usoskin, 2010; Masarik and Beer, 2009; Webber et al., 2007) and have been applied on a global scale to study the atmospheric production, transport, mixing and deposition processes of meteoric ^{10}Be . When applied to the local (e.g. pedon or small river catchment) scale, however, GCM-derived depositional fluxes might be non-representative, given the low horizontal resolution of e.g. 2.8×2.8 degrees that often does not allow to resolve local topographic or climatic gradients (Dixon et al., 2018). In comparison, ^{10}Be measurements in natural materials can provide site-specific ^{10}Be depositional fluxes. Contemporary depositional fluxes can be determined by measuring meteoric ^{10}Be concentrations in rain with known precipitation rates (Graham et al., 2003; Monaghan et al., 1986), but such values are only representative over the sampling period, rather than over geomorphically meaningful timescales (10^3 - 10^5 yrs).

Over millennial scales, the meteoric ^{10}Be inventory in dated soil profiles developed from river terraces, moraine deposits, or bedrock, can provide a site-specific, long-term average depositional flux (Graly et al., 2011). Even though in quite a few studies meteoric ^{10}Be was measured in soil (e.g. Bacon et al., 2012; Jungers et al., 2009; Mckean et al., 1993), most of them aimed at exploring the vertical and lateral transport of ^{10}Be , and only very few studies estimated the depositional processes of ^{10}Be (Clow et al., 2020; Dixon et al., 2018; Ouimet et al., 2015; Reusser et al., 2010). This is because several prerequisites have to be met for determining site-specific ^{10}Be deposition fluxes using dated soil profiles: 1) Full retention of meteoric ^{10}Be since landform stabilization. The assumption of full retention (Bacon et al., 2012; Maher and von Blanckenburg, 2016) may be invalid when meteoric ^{10}Be mixes and remobilizes within soil profiles and desorption may occur, depending on soil properties and ages (Graly et al., 2010; Schoonejans et al., 2017). 2) No removal of Be isotopes by surface erosion. This assumption is not met if the slope of the studied outcrop is steep or agricultural activities are prominent (Jelinski et al., 2019; Johnson et al., 2014). 3) Negligible or known meteoric ^{10}Be inherited prior to landform

stabilization. Regarding alluvial substrates, ignoring such inherited ^{10}Be can cause overestimation of its inventory (Egli et al., 2010).

To evaluate the abovementioned assumptions on soil ^{10}Be , chemical properties such as soil pH and ^9Be can provide independent constraints. A low soil pH (e.g. <5) indicates the potential of partial retention of ^{10}Be , meaning the desorption of Be from particles and its loss to the dissolved phase (You et al., 1989). Stable ^9Be is released during chemical weathering of primary minerals, and bound to secondary reactive minerals in soil similar to ^{10}Be (Bacon et al., 2012; Schoonejans et al., 2017), but the difference in sources causes distinct and predictable distribution patterns of both isotopes with depth (Maher and von Blanckenburg, 2016). In young deposits (e.g. Holocene terraces), ^{10}Be concentrations with depth often show a declining profile that is controlled by downward transport and adsorption processes (Willenbring and von Blanckenburg, 2010); the fraction of ^9Be locked in primary minerals ($[^9\text{Be}]_{\text{min}}$) shows an increasing trend with depth as mineral weathering is the strongest at the surface (Maher and von Blanckenburg, 2016); the fraction of ^9Be enriched in secondary reactive minerals ($[^9\text{Be}]_{\text{reac}}$) commonly shows a convex profile, affected by chemical leaching at the surface and the limit of illuviation processes at depth (Maher and von Blanckenburg, 2016). As such, the chemical mobility of ^{10}Be within soil profiles can be evaluated when coupling depth variations of both Be isotopes.

In this study, we focus on the Taiwan mountain belt, which is of high interest for Earth surface studies because it is one of the fastest-eroding settings (on the order of 1-10 mm/yr) in the world (Cook et al., 2014; Dadson et al., 2003; Hilton et al., 2008). The commonly used *in situ* cosmogenic ^{10}Be in quartz for quantifying Earth surface processes is not readily applicable in such a rapidly eroding setting given its low concentrations at the surface, whereas meteoric ^{10}Be is more suitable due to its higher abundance and its independence on substrate lithology (Deng et al., 2020b; Derrieux et al., 2014). We analyzed meteoric ^{10}Be and stable ^9Be in river terrace profiles formed during the Holocene on the eastern and western sides of the orogen. Our aim is to constrain the range of Holocene ^{10}Be depositional

fluxes in the Taiwan orogen, compare this with other independent flux estimates from fitting rainfall records and GCM modelling, and evaluate potential causes of bias in each of them.

2. Study area

Due to the active collision between the Luzon Arc and the Asian continental margin since ~6 Ma (Huang et al., 2006), the Taiwan orogen has undergone rapid tectonic uplift with rates of 4 – 10 mm/yr in the last ~1 Ma (Hsu et al., 2016; Lee et al., 2006), and 10 – 15 mm/yr in modern times (Ching et al., 2011) in the orogen's metamorphic core (the Central Range; Fig. 1). The orogen has a tropical-subtropical climate dominated by East Asian monsoon, and receives a mean annual rainfall of 2.5 m, a large fraction of which is brought by tropical typhoons (Wu and Kuo, 1999).

Triggered by heavy rains or large earthquakes, the Taiwan orogen is subject to high-frequency landsliding (Hovius and Lin, 2000; Hovius et al., 2011), which supplies enormous amounts of sediment downslope. As a result, rivers draining the orogen typically have extremely high sediment yields (e.g., $>10^4$ t/km²/yr) (Kao and Milliman, 2008; Milliman and Farnsworth, 2011). Where sediment supply carried by large landslides exceeds the transport capacity, valleys aggrade, along with the development of alluvial/debris fans in otherwise incision-dominated bedrock-river systems (Hartshorn et al., 2002). Such an episodic change in river behaviour is observed in modern times (Hsieh and Capart, 2013), as well as recorded by the presence of Quaternary alluvial-fan terraces that are common in/around the orogen (Hsieh and Chyi, 2010; Hsieh et al., 2011). These terraces are sometimes underlain by fluvial or debris-flow gravels as thick as >100 m and capped by weakly developed soils. Hundreds of radiocarbon dates (mostly <15 ka) have shown that these terraces were deposited in relatively short periods of time of generally less than several hundred years (Hsieh and Chyi, 2010; Hsieh et al., 2017).

3. Materials and methods

3.1. Terrace deposit sampling

Even though abundant terraces exist in the Taiwan orogen, accessibility and existence of terrace chronology are problematic. Often, ages of most terraces older than 1 ka dated by previous studies were derived only from the lower parts of the terraces, thus not accounting for the remaining terrace bodies rising commonly > 20 m high above riverbeds. In addition, the tops of the terraces were either difficult to reach or poorly exposed during our survey periods. Still, we rappelled and collected samples from the topmost 6.2 m-thick deposits overlying the ~150 m-high Xinxiang (XX) fan terrace exhibited along the Chenyoulan River in central Taiwan (Fig. 1). The XX terrace, constructed jointly by three tributaries, extends for 7 km along the trunk river and consists entirely of gravelly sediment. The main part of this deposit consists of ~120 m of greyish gravel deposits, presumably of debris-flow origin, and has yielded 5 radiocarbon dates from residual plant material and ranging from 9.30 to 8.80 kyr cal. BP (calibrated in years before 1950 AD) (Hsieh and Chyi, 2010). Around the sampling segment from the top, the terrace is capped by yellowish debris-flow gravel of ~10 m thickness. Our samples are all derived from this yellowish unit, which has a sharp boundary with the underlying greyish gravel.

We also collected samples from the Shengguang (SG) fan terrace, a 3.2 m-high minor terrace in the upper Dajia River catchment, central-northern Taiwan (Fig. 1). This terrace is dominated by fluvial gravel. The sampled segment has yielded 3 radiocarbon dates ranging from 3.57 to 4.08 kyr cal. BP.

Finally, we sampled the topmost 5.9 m of the Changbin (CB) fan terrace in eastern Taiwan (Fig. 1), from a drill core obtained by the Central Geological Survey of Taiwan in 2006 (Hsieh et al., 2011). The deposits sampled from bottom to top include muddy debris-flow and peaty mud; both units have yielded 7 radiocarbon dates from e.g. peat and charcoal and ranging from 7.70 to 6.44 kyr cal. BP (Hsieh et al., 2017; Hsieh et al., 2011).

3.2. Measurement of soil pH and bulk density

Soil pH (derived from 0.01 M CaCl₂) was determined on the sieved <2 mm fraction of air-dried samples using a soil-solution ratio of 1:2. For each profile, three additional samples were collected from top to bottom using a steel cylinder of known volume (100 cm³); these oven-dried samples were weighed to obtain the bulk density.

3.3. Extraction of ¹⁰Be and ⁹Be

We extracted ¹⁰Be and ⁹Be from the oven-dried fine fraction (<2 mm) of all samples based on the sequential chemical extraction procedure described in Wittmann et al. (2012). After gentle grinding that aimed at breaking up secondary grain sizes formed during oven-drying, 0.3-0.5 g of each sample was treated subsequently with 0.5 M HCl for extracting the amorphous oxyhydroxide fraction, and then with 1M hydroxylamine-hydrochloride solution for the crystalline oxyhydroxide fraction. These fractions contain amorphous and crystalline oxyhydroxides that were then combined as the reactive fraction (termed as “reac”) for measuring stable ⁹Be and meteoric ¹⁰Be concentrations. After these sequential extraction steps, the residue (termed “min”) was decomposed with a mixture of hydrofluoric acid and aqua regia.

After matrix decomposition, the reactive and residual solute fractions were split. One split was analyzed for stable ⁹Be concentrations by Inductively Coupled Plasma-Optical Emission Spectroscopy (ICP-OES, Varian 720-ES). The second split of all the reactive fractions and selected (i.e. the surface and bottom samples of each profile) residual fractions were spiked with ⁹Be carrier of known weight and purified for ¹⁰Be analysis by performing anion and cation column separation and alkaline precipitation (e.g. von Blanckenburg et al., 1996). ¹⁰Be concentrations were obtained from accelerator mass spectrometry (AMS) measurements of ¹⁰Be/⁹Be ratios (with carrier) at the University of Cologne relative to the KN01-6-2 standard with a ¹⁰Be/⁹Be ratio of 5.35×10^{-13} (Dewald et al., 2013). For blank correction of ¹⁰Be concentrations we used a blank ¹⁰Be/⁹Be ratio of $0.74 \pm 0.21 \times 10^{-15}$ (n=2) for reac fractions and $8.32 \pm 1.30 \times 10^{-15}$ (n=1) for min fractions, respectively.

3.4. Calculation of ^{10}Be depositional flux

The ^{10}Be inventory accumulating after terrace formation can be calculated using the following equation (modified from Egli et al. (2010)):

$$I_{10} = \sum_{i=1}^n ([^{10}\text{Be}]_{\text{bulk},i} - [^{10}\text{Be}]_{\text{inh}}) \times \rho_i \times z_i \times V_{f,i} \quad (1)$$

Where I_{10} represents the total ^{10}Be inventory in a soil column corrected for ^{10}Be inheritance (at/m^2), $[^{10}\text{Be}]_{\text{bulk},i}$ the total ^{10}Be concentration in each sample (at/kg), $[^{10}\text{Be}]_{\text{inh}}$ the ^{10}Be concentration in each profile inherited from the previous erosion process (at/kg), ρ_i the soil bulk density (kg/m^3), z_i the integrated thickness of the i^{th} horizon (m), and $V_{f,i}$ the volume percentage (%) of the fine earth fraction ($<2 \text{ mm}$) containing ^{10}Be . The parameters in Eq. (1) were obtained as follows.

1) To determine the ^{10}Be inherited from the erosion event that formed the terrace ($[^{10}\text{Be}]_{\text{inh}}$), two approaches were applied: (1a) using the ^{10}Be concentration of modern river sediment obtained close to the terrace location, or (1b) using the ^{10}Be concentration measured at the bottom of the terrace profile that is unaffected by meteoric ^{10}Be delivery since terrace deposition.

2) In most samples we only measured meteoric ^{10}Be in reactive fractions where the majority of ^{10}Be is contained. However, a small fraction of ^{10}Be can be contained in the silicate residual “min” fraction after chemical leaching (Simon et al., 2016; Wittmann et al., 2012). This observation may be explained by non-quantitative extraction of reactive ^{10}Be in oxyhydroxides by the leaching procedure or ^{10}Be contribution of secondary clay minerals that can not be decomposed by the leaching procedure. From a few samples in which both the reac and the min fractions were measured we determined the mean fraction of reactive ^{10}Be relative to bulk ^{10}Be ($f_{\text{reac-10}}$). We hence divided the reactive ^{10}Be ($[^{10}\text{Be}]_{\text{reac}}$) in each sample by this fraction to account for contribution of “min” ^{10}Be and obtain $[^{10}\text{Be}]_{\text{bulk}}$.

3) The soil thickness integrated by each sample (z_i) was determined as the distance from the mid-point between sample _{$i-1$} and sample _{i} to the mid-point between sample _{i} and sample _{$i+1$} ; at the bottom of

each profile, an additional sample thickness, being the same as the distance from the mid-point between sample_{bottom-1} and sample_{bottom} to sample_{bottom}, was added below for calculating ¹⁰Be inventory.

4) Based on field observations (see Fig. 2), terraces XX and SG contain a certain percentage of gravel and boulders. Due to the low specific surface area of such large particles, particles with a diameter of >2 mm accumulate a negligible amount of ¹⁰Be relative to finer-grain soil material (Willenbring and von Blanckenburg, 2010). Hence, z_i in Eq. (1) should be corrected by removing such coarse fractions, that is, multiplied by the volume percentage of the fine earth fraction (<2 mm) containing ¹⁰Be (V_f). In practice, we used a two-step approach to separate the coarse fraction (>2 mm) from the fine earth fraction containing ¹⁰Be. 1) The >2 mm fraction contained in the collected samples was determined by sieving (using a 2 mm sieve) and weighing the corresponding fractions. The weight percentage of the >2 mm fraction that is dominated by rock fragments was then converted to volume percentage (V_{c1}) by assuming a density of 2.65 g/cm³ common for sedimentary rocks. 2) As the unsampled boulders in the profile commonly had a diameter of >6 cm in our case, we manually extracted their area percentage from photos of each profile (Fig. 2a-b) using GIS mapping software (ArcMap). Next, the area percentage (ellipse area of boulders divided by rectangle area of profile) was converted to the volume percentage (V_{c2} , ellipsoid volume divided by cube volume), that is, multiplied by a factor of 2/3. The resulting V_f in Eq. (1) is calculated by combining the two steps of correction:

$$V_f = (1 - V_{c2}) \times (1 - V_{c1}) \quad (2)$$

The terrace-derived meteoric ¹⁰Be depositional flux F_{met} (at/m²/yr) is then calculated as:

$$F_{\text{met}} = I_{10} \times \lambda / (1 - e^{-\lambda t}) \quad (3)$$

where t (yr) is the depositional age of the terrace derived from an independent method, in this case from radioactive ¹⁴C, and λ is the decay constant of ¹⁰Be ($5 \times 10^{-7} \text{ yr}^{-1}$). The uncertainty of the resulting F_{met} is propagated from the analytical uncertainty of ¹⁰Be measurements, the ¹⁴C age uncertainty, the standard deviation of soil density measurements, and a relative standard deviation of 5% from obtaining

V_f . The calculation of F_{met} assumes that ^{10}Be is completely retained since terrace deposition and may represent a lower-limit estimate in many cases.

3.5. Correction for ^{10}Be loss from desorption

Be desorption can occur under low soil pH conditions which leads to an underestimation of ^{10}Be inventory. To estimate such inventory loss, one approach is to use the mass loss percentage of reactive ^9Be to constrain the chemical depletion of ^{10}Be , assuming that the retention of reactive ^9Be and ^{10}Be within soil profiles is the same (Bacon et al., 2012; Schoonejans et al., 2017). Nevertheless, ^{10}Be is supplied from the surface while ^9Be is released at the weathering front. As such, incomplete retention may affect each of both isotopes to a different extent due to difference in sources (Maher and von Blanckenburg, 2016).

The other approach developed here is a partition coefficient (K_d)-based estimation of inventory loss. The pH-dependent K_d (in L/kg) of Be is calculated by the ratio of reactive to dissolved Be concentrations at chemical equilibrium (You et al., 1989), which provides an estimate of the potential loss of Be to the dissolved phase due to desorption. Taking the soil column as a whole and assuming a constant pH over time, the change in ^{10}Be inventory at a given time is the deposition of meteoric ^{10}Be from the surface minus the removal of ^{10}Be from the soil column due to desorption; when integrating from the terrace depositional age (t) to present-day, we can then derive the loss percentage of ^{10}Be inventory ($I_{10,\text{loss}}$). The conceptual framework and the equation for ^{10}Be desorption loss correction is provided in Appendix A.

4. Results

Soil pH and bulk density data are provided in Table 1. The soil pH in terrace XX decreases from 4.83 to 3.85 within the top 0.2 m, and then gradually increases to 6.09 at 6.2 m. The soil pH in terrace SG decreases from 7.02 to 3.85 within the top 1 m, and then increases to 4.91 at 3.2 m. Circum-neutral

soil pH prevails in terrace CB, ranging from 5.60 to 7.00. For each profile the bulk density of surface soil is always lower than that of samples attained from depth (Table 1). The range of bulk density in each profile is 0.86-1.09 g/cm³ (XX), 0.76-1.78 g/cm³ (SG) and 1.32-2.08 g/cm³ (CB), respectively. The bulk density of the surface layer is measured including a relative uncertainty of 10%. To assign a density value to each subsurface terrace layer, we use the average value of the two density measurements taken below the surface as bulk density, including an uncertainty of the standard deviation of both measurements. The assigned density values are shown in Table 1.

¹⁰Be and ⁹Be concentrations of reac and min fractions with depth are shown in Figs. 3-5 and Table 2. In terraces XX and CB, [¹⁰Be]_{reac} generally decreases with depth, from 40.56×10⁶ at/g to 6.50×10⁶ at/g (XX, Fig. 3) and from 68.34×10⁶ at/g to 0.47×10⁶ at/g (CB, Fig. 5). In contrast, the [¹⁰Be]_{reac} in terrace SG decreases from 24.85×10⁶ at/g to 1.57×10⁶ at/g within the top ~1 m, but then increases again to 7.64×10⁶ at/g with increasing depth (Fig. 4). From replicates taken from different locations at the surface (labelled “0 m” in Table 1), the surface average [¹⁰Be]_{reac} ± 1σ is 36.98 ± 5.06×10⁶ at/g in terrace XX, 23.26 ± 2.25×10⁶ at/g in terrace SG, and 66.80 ± 2.18×10⁶ at/g in terrace CB. The low standard deviation indicates good spatial replicability of surface soils. Similar to [¹⁰Be]_{reac}, the bulk ¹⁰Be concentration ([¹⁰Be]_{bulk}, sum of reac and min fractions, Table 2) of the surface sample is always much higher than that at the bottom for each profile. In general, the [¹⁰Be]_{reac} accounts for most of [¹⁰Be]_{bulk} (71%-86%), the only exception being the [¹⁰Be]_{reac} at the bottom of terrace CB, where [¹⁰Be]_{reac} accounts for only 44.3% of [¹⁰Be]_{bulk}. We regard the resulting f_{reac-10} in this sample as an outlier given that [¹⁰Be]_{reac} is extremely low (0.47×10⁶ at/g) in this sample and [¹⁰Be]_{reac} of all the other analyzed samples ranges within 10⁶-10⁷ at/g. Hence, we use the average ratio of [¹⁰Be]_{reac} to [¹⁰Be]_{bulk} in terraces XX and SG (78.2%, n=4) as a reasonable estimate of f_{reac-10}.

[⁹Be]_{reac} shows a different distribution pattern with depth compared to [¹⁰Be]_{reac} (Figs. 3-5). In terrace XX, [⁹Be]_{reac} is characterized by a convex profile, with [⁹Be]_{reac} increasing from 0.39 µg/g to 0.82 µg/g within the top 0.80 m and then decreasing to 0.59 µg/g. In terrace SG, [⁹Be]_{reac} fluctuates at

the top 2.4 m but overall increases from 0.58 $\mu\text{g/g}$ to 1.07 $\mu\text{g/g}$, and then decreases to 0.84 $\mu\text{g/g}$ at the bottom. In terrace CB, $[\text{}^9\text{Be}]_{\text{reac}}$ shows a declining profile from 0.29 $\mu\text{g/g}$ at the surface to 0.11 $\mu\text{g/g}$ at depth. In general, $[\text{}^9\text{Be}]_{\text{min}}$ is the highest in terrace SG (Fig. 4) and the lowest in terrace CB (Fig. 5), consistent with the trend in $[\text{}^9\text{Be}]_{\text{reac}}$. In terrace XX, $[\text{}^9\text{Be}]_{\text{min}}$ increases from 0.66 $\mu\text{g/g}$ to 1.15 $\mu\text{g/g}$ at the top 0.80 m and then stays relatively constant with depth ($1.14 \pm 0.03 \mu\text{g/g}$, $n=6$, Fig. 3). $[\text{}^9\text{Be}]_{\text{min}}$ in terrace SG generally increases with depth from 0.89 $\mu\text{g/g}$ to 2.01 $\mu\text{g/g}$ (Fig. 4), whereas $[\text{}^9\text{Be}]_{\text{min}}$ remains stable ($0.23 \pm 0.03 \mu\text{g/g}$, $n=8$) in the whole CB profile, except one value of 0.42 $\mu\text{g/g}$ at 0.51 m (Fig. 5).

5. Discussion

5.1. Depth-related controls of ^9Be and ^{10}Be concentrations

When coupling the depth profile of ^{10}Be to those of ^9Be and soil pH, we can determine the controlling factors of remobilization of Be isotopes within soil profiles and further evaluate the retention of ^{10}Be . In terrace XX the vertical distribution of ^9Be is consistent with the weathering mechanism. The increase of $[\text{}^9\text{Be}]_{\text{min}}$ with depth (in the upper ~ 0.8 m, Fig. 3) is caused by weaker dissolution of primary minerals towards the bottom, whereas the lower $[\text{}^9\text{Be}]_{\text{reac}}$ at near-surface is due to the low soil pH and thus low Be retentivity there. At depths below ~ 0.8 m, the uniformity in $[\text{}^9\text{Be}]_{\text{min}}$ indicates insignificant dissolution of primary minerals (Maher and von Blanckenburg, 2016). In comparison, high $[\text{}^{10}\text{Be}]_{\text{reac}}$ at the surface and its subsequent decrease with depth (Fig. 3) is related to the supply of meteoric ^{10}Be from the surface followed by downward transport through fluid flow. The constantly low $[\text{}^{10}\text{Be}]_{\text{reac}}$ below 3.2 m ($6.93 \pm 0.37 \times 10^6 \text{ at/g}$, $n=3$) suggests that this ^{10}Be concentration is inherited from the river sediment prior to deposition, rather than from post-depositional accumulation and downward transport.

In terrace SG the increasing $[\text{}^9\text{Be}]_{\text{min}}$ in the upper 2.4 m relative to the constant value of 2.0 $\mu\text{g/g}$ below this depth also suggests a main control of primary mineral dissolution on its distribution (Fig. 4). The increase of $[\text{}^9\text{Be}]_{\text{reac}}$ in the upper 2.4 m (Fig. 4) is consistent with an increase in Be retentivity there. Similar to terrace XX, the pattern of $[\text{}^{10}\text{Be}]_{\text{reac}}$ generally reflects expected trends of high ^{10}Be

concentrations at the surface due to atmospheric supply, followed by much lower $[^{10}\text{Be}]_{\text{reac}}$ at depth. However, the low soil pH (3.85-3.92) at depths of 1.0-1.9 m (Fig. 4) that results in low retentivity of ^{10}Be (You et al., 1989) may lead to further downward transport of dissolved ^{10}Be at depth where the pH is higher (4.91). At these depths, $[^{10}\text{Be}]_{\text{reac}}$ increases in accordance to changes in pH-related retentivity that controls the formation of secondary minerals (Graly et al., 2010; Maher and von Blanckenburg, 2016).

For terrace CB, $[^9\text{Be}]_{\text{min}}$ is relatively constant with depth, indicating minor chemical alteration of primary minerals in the sampled profile (Fig. 5). The co-variation and the similar declining trend of both $[^{10}\text{Be}]_{\text{reac}}$ and $[^9\text{Be}]_{\text{reac}}$ suggests, in contrast to the other profiles, significant surface erosion as the upper part of the profile with high $[^{10}\text{Be}]_{\text{reac}}$ and low $[^9\text{Be}]_{\text{reac}}$ (Maher and von Blanckenburg, 2016) is eroded. As a result, the variations of $[^{10}\text{Be}]_{\text{reac}}$ and $[^9\text{Be}]_{\text{reac}}$ in the remaining lower part of the soil column are dominated by illuviation processes, meaning the gradual re-formation of reactive phases that are sourced from the leaching of reactive phases in the original top-soil (missing in terrace CB due to erosion). Concentrations of both isotopes then increasingly reflect the influence of parent materials with depth.

The depth profile of ^{10}Be can also help to determine its inheritance in each terrace, which is a key parameter for correction of ^{10}Be inventory in Eq. (1). In terrace XX, given that $[^{10}\text{Be}]_{\text{reac}}$ below 3.2 m is invariant with depth (Fig. 3), the mass-weighted $[^{10}\text{Be}]_{\text{reac}}$ of the bottom three sampled layers is assumed to represent the inheritance (i.e., 6.97×10^6 at/g). Furthermore, since inherited ^{10}Be is sourced from the erosion event that formed the terrace, we can use the Be isotopic dataset of the bottom layers to determine a paleo-denudation rate. Following the framework of the ^{10}Be (meteoric)/ ^9Be denudation proxy (von Blanckenburg et al., 2012) and using the same parameterization applied for the modern Chenyoulan River by Deng et al. (2020b) (see Appendix B for details), the resulting denudation rate of the Chenyoulan Basin in the early Holocene is 0.51 ± 0.03 mm/yr ($n=3$). This paleo-denudation rate is lower than that in the modern times (1.01 ± 0.20 mm/yr, Deng et al. (2020b)), indicating potential

acceleration of sediment removal through the Holocene. Similarly for terrace CB, we assume the $[^{10}\text{Be}]_{\text{reac}}$ value at the bottom of the terrace to be the inherited signal (0.47×10^6 at/g) due to its extremely low concentration (Fig. 5). In terrace SG, an increase of $[^{10}\text{Be}]_{\text{reac}}$ in the lower profile (Fig. 4) makes identifying a value for inherited ^{10}Be difficult. To constrain ^{10}Be inheritance in terrace SG, we adopted a published $[^{10}\text{Be}]_{\text{reac}}$ value (0.81×10^6 at/g) from a modern sediment sample in the Zhuoshui headwaters nearby (Deng et al., 2020b, Fig. 1). We consider the choice of this ^{10}Be inheritance to be reasonable as erosion rates (and presumably $[^{10}\text{Be}]$) in both locations should be similar because: 1) the Zhuoshui sediment (ZS-1) is sourced from a sub-catchment with similar geological (slate lithology) and topographic (Central Range) features as the Dajia headwaters, hinting at a similar erosion process; 2) the exhumation rate of 3 mm/yr since ~ 1 Ma (Hsu et al., 2016) determined in a transect of the northern Central Range (only ~ 20 km away from terrace SG) is indeed close to the denudation rate of ZS-1 (3.8 ± 0.7 mm/yr) (Deng et al., 2020b).

More importantly, the variations of both Be isotopes suggest incomplete Be retention and surface erosion in certain profiles and hence the violation of the assumption of a complete ^{10}Be inventory since terrace deposition. These factors will be evaluated below to derive a better estimate on ^{10}Be depositional flux.

5.2. Terrace-derived ^{10}Be depositional fluxes and evaluation of potential uncertainties

^{10}Be inventories of the three terraces are calculated based on Eq. (1) using chemical and physical data provided in Table 1 and Table 2. The resulting ^{10}Be depositional fluxes derived from Eq. (3) and corrected for ^{10}Be inheritance are provided in Table 3. In brief, the ^{10}Be depositional flux calculated from terrace XX is 0.32×10^6 at/cm²/yr, which is lower than the flux values derived from terraces SG and CB that range between 0.45 - 0.49×10^6 at/cm²/yr (Table 3).

Next, we consider a range of scenarios in Taiwan terraces that may lead to violation of assumptions on deriving ^{10}Be depositional flux from soil profiles, and then evaluate their effect on resulting flux estimates. The scenarios include 1) low Be retentivity, and terrace properties such as 2) surface erosion, 3) multi-phase sediment deposition and 4) incomplete sampling depth. Based on reasons summarized below (Table 4), these scenarios affect each terrace to a different extent.

1) Partial retention, meaning the desorption of Be from particles and its loss to the dissolved phase, should be taken into account when soil pH is low. In terrace CB, the soil pH is generally around or above 6 (Fig. 5) and thus ^{10}Be in soil is considered to be retained completely. In contrast, the upper part (depth $< \sim 1.2$ m) of terrace XX and the lower part (depth $> \sim 1$ m) of terrace SG show a soil pH lower than 5, which makes partial loss of ^{10}Be likely. When correcting the ^{10}Be inventory for desorption loss, a higher ^{10}Be depositional flux will result for terraces XX and SG (see Sections 5.2.1 and 5.2.2 and Fig. 6).

2) Surface erosion should be insignificant in terraces of which the flat surfaces were well-preserved. We observed no obvious field signs of soil removal from the top for terraces XX and SG. Nevertheless, as mentioned in Section 5.1, the co-variation and the similar declining trend of both $[^{10}\text{Be}]_{\text{reac}}$ and $[^9\text{Be}]_{\text{reac}}$ in profile CB does suggest significant surface erosion. Hence, adding a missing ^{10}Be inventory from the eroded top soil will increase the calculated ^{10}Be depositional flux for terrace CB (Section 5.2.3 and Fig. 7).

3) The depositional ages of collected SG and CB sediments are considered to be well-constrained as several dating points ($n=3$ for SG and $n=7$ for CB) are available for the sampled segments. However, the thickness of terrace XX is ~ 150 m and the dating points ($n=5$) are limited to the lower part (Site 11 in Hsieh and Chyi (2010)) unsampled for Be isotopes. Hence, the depositional age at the top 6.2 m where our samples were taken may be younger and thus, according to Eq. (3), a realistic depositional flux should be higher for terrace XX (Fig. 6).

4) Incomplete sampling, meaning that the sampling depth is not deep enough to reach the ^{10}Be inheritance signal and a part of the ^{10}Be inventory may be missing, might be the cause of an underestimate of the inventory in terrace SG where the lower part (depth of 1-3.2 m) shows a gradual increase of $[\text{}^{10}\text{Be}]_{\text{reac}}$. Extending the sampling depth to a deeper level will result in an increased ^{10}Be inventory and thus a higher ^{10}Be depositional flux (Fig. 6).

In consideration of these different kinds of scenarios, the ^{10}Be depositional flux that we derived from our terrace profiles is indeed a lower-bound estimate. Next, we will evaluate effects of soil pH and depositional age for terrace XX (Section 5.2.1), effects of soil pH and unsampled depth for terrace SG (Section 5.2.2), and for terrace CB, surface erosion is considered as the main cause (Section 5.2.3).

5.2.1. Terrace XX

To derive a realistic range of ^{10}Be depositional flux from terrace XX, we estimate the pH-dependent desorption loss of the ^{10}Be inventory using Eq. (A.3) and the age-dependent ^{10}Be flux using Eq. (3) according to the following parameter constraints (Table 4):

1) The depositional age in Eqs. (3) and (A.3) is set to be younger than 9.05 ka (Table 3).

2) To obtain a profile-scale K_d in Eq. (A.3) we calculated a mass-weighted pH (4.62) based on the soil pH and the mass of the <2 mm fraction for each sampled layer above the inheritance (mid-point of XX6 and XX7). The resulting profile-scale desorption rate represents a lower limit, however, because most loss likely occurs in the upper part of the profile where concentrations are highest and pH is lowest. To account for this effect we vary pH values in a range from 3.85 (the lowest pH in the profile) to 4.62 (Fig. 6a). Within the given range of pH and depositional ages, the range of desorption-related $I_{10,\text{loss}}$ is 8% to 76%, higher than the proportion of bulk ^9Be loss in the profile (0.2%). Bulk ^9Be loss is the difference between initial terrace ^9Be inventory calculated by assuming a constant $[\text{}^9\text{Be}]_{\text{bulk}}$ as the 3 samples at the bottom and ^9Be inventory calculated by the measured $[\text{}^9\text{Be}]_{\text{bulk}}$ profile and indicates the total loss of ^9Be to the dissolved pool. Bulk ^9Be loss is controlled by both desorption and primary

mineral dissolution, and the latter process is much slower compared to desorption (Maher and von Blanckenburg, 2016). Hence $I_{10,loss}$ higher than the bulk ^{10}Be loss (%) is expected.

The response of modelled ^{10}Be depositional fluxes from terrace XX to ranges in depositional age and soil pH obtained from the above-made assumptions is shown in Fig. 6a. As expected, lower pH and younger depositional ages result in a higher modelled depositional flux (Fig. 6a). Using this modelling approach, we derive modelled ^{10}Be fluxes that must exceed a value of 0.66×10^6 at/cm²/yr (red start in Fig. 6a) within the given range of pH values (<4.62). Furthermore, based on existing ^{14}C -dated terraces in the Chenyoulun River, the calculated fan incision rate from old terraces (>1 ka) should be 8-31 m/ka (n=5) (Hsieh and Chyi, 2010). The upper-bound incision rate, if applicable in terrace XX (thickness: ~150 m), indicates a minimum terrace age of 4.84 ka. Accordingly, the maximum modelled ^{10}Be flux varies within a range of 0.94 - 2.26×10^6 at/cm²/yr depending on soil pH (Fig. 6a).

5.2.2. Terrace SG

In terrace SG we estimate a modelled ^{10}Be inventory and flux according to the depth-dependent inventory calculation using Eq. (1) and the pH-dependent desorption loss of the ^{10}Be inventory using Eq. (A.3), based on the following parameter constraints (Table 4):

1) For the unsampled section below 3.2 m, we assume that its physical properties (e.g. density and fine earth fraction) are the same as those of the deepest sample (SG9) and the ^{10}Be concentration linearly decreases from 3.2 m until reaching the assumed inheritance value of 0.81×10^6 at/g (Section 5.1). Note that this is a conservative estimate considering that ^{10}Be concentrations could still increase below 3.2 m, although the increasing pH at this depth (Fig. 4) suggests that leaching processes will gradually play a minor role. Under these assumptions, the missing inventory is then a function of the unsampled depth having an average ^{10}Be concentration of SG9 and the assumed inheritance value (Table 3).

2) Similar to terrace XX, a representative profile-scale soil pH is needed for estimating the ^{10}Be loss from desorption using Eq. (A.3). Nevertheless, the resulting profile-scale desorption rate using

mass-weighted pH (4.68) represents an upper limit as less loss likely occurs in the upper part of the profile where both $[^{10}\text{Be}]_{\text{reac}}$ and pH are highest. To account for this effect we vary pH values in a range from 4.68 to 7.02 (the highest pH in the profile) (Fig. 6b). In contrast to terrace XX, the range of desorption-related $I_{10,\text{loss}}$ is <1% to 13% within the given range of pH and unsampled depth, and the bulk ^9Be loss (7%) falls within this range. It indicates that desorption in terrace SG may play a secondary role in evaluation of ^{10}Be inventory given the higher profile-scale pH (>5) and thus the small horizontal gradient in color in Fig. 6b.

Overall, the modelled ^{10}Be depositional flux increases with lower soil pH and larger unsampled depth (Fig. 6b). Besides, based on the well-constrained infiltration depths of ^{10}Be of our other Taiwan Holocene terraces (Fig. 3 and Fig. 5), we infer that the maximum infiltration depth in terrace SG should not exceed 6 m. An infiltration depth of 6 m would then correspond to an unsampled depth of 2.8 m, and a modelled flux of $0.80\text{--}0.88 \times 10^6$ at/cm²/yr would result for terrace SG within the given pH range (Fig. 6b).

5.2.3. Terrace CB

In terrace CB we model the variations in ^{10}Be depositional flux as a function of eroded soil thickness (Fig. 7) following a strategy similar to Clow et al. (2020). To constrain the ^{10}Be concentration in the eroded surface soil ($[^{10}\text{Be}]_{\text{surface}}$), two scenarios are considered here:

1) We extrapolate the decreasing trend of ^{10}Be concentration with depth at the top ~0.22 m (Fig. 5) to the eroded soil segment, resulting in a positive correlation between $[^{10}\text{Be}]_{\text{surface}}$ and the thickness of eroded soil (scenario ① in Fig. 7). The underlying assumption is that the soil profile is not well-developed and its upper part has been removed by erosion recently (e.g. in recent decades).

2) Assuming a mixed layer that has developed in the upper soil due to bioturbation, a constant $[^{10}\text{Be}]_{\text{surface}}$ same as that of the surface sample (CB-surface and CB1C) is used (scenario ② in Fig. 7).

Since no independent erosion estimates exist for terrace CB, we assume that the erosion rate may vary within a range similar to the Pakua terraces of western Taiwan (3-30 mm/kyr) where erosion rates are well-constrained by *in situ* ^{10}Be depth profiles (Siame et al., 2012). When using the highest erosion rate as an upper-bound limit for terrace CB, modelled depositional fluxes of 0.80×10^6 and 0.93×10^6 at/cm²/yr result for scenarios 2 and 1, respectively. Although such assumption on the maximum erosion rate might not be necessarily valid, the lower limit as the measured terraced-derived flux can still help to constrain the realistic flux range in this orogen.

5.3. Comparison between ^{10}Be flux estimates by multiple approaches

Here we aim to derive a better constrained ^{10}Be depositional flux in the Taiwan orogen by 1) comparing between the plausible range of ^{10}Be flux from each terrace and then 2) comparing terrace-derived fluxes with independent estimates from GCM integrating over the Holocene (Heikkilä and von Blanckenburg, 2015) and from a rainfall ^{10}Be -based fitting equation (including precipitation rate and latitude as parameters) (Graly et al., 2011). For the latter we use modern precipitation rates (Table 3) to calculate the ^{10}Be flux. We consider that the temporal variability in precipitation rate may be relatively small because the Taiwan orogen is dominated by subtropical-wet climate consistently during the study period (9-0 kyr BP) based on pollen records (Liew et al., 2006). Few dry or wet episodes on a timescale of $\sim 10^2$ years occurred during the Holocene (Liew et al., 2006) but their effect should be averaged out over the integration timescale of terrace profiles. Fluxes from modern rainfall data fitting are further normalized to the average Holocene ^{10}Be production rate (Deng et al., 2020a) for comparison with other two approaches.

Key controlling factors of ^{10}Be depositional flux include temporal variations in stratospheric ^{10}Be production and the mechanisms of its delivery that depend on climatic effects such as precipitation (Graly et al., 2011; Heikkilä et al., 2013b). We first evaluate how these factors might have caused difference in flux estimates between terraces. According to proxy records of global ^{10}Be production

(Steinhilber et al., 2012), the ^{10}Be production rate within the depositional age of each terrace is 1.16-1.23 times that of the modern value (Fig. 8). In other words, given this narrow range the time-averaged ^{10}Be production rate should be in agreement between terraces. The effect of precipitation on soil-derived ^{10}Be depositional flux is a matter of debate (Deng et al., 2020a). One group of studies suggested that the ^{10}Be depositional flux is positively correlated with precipitation rate, and that this precipitation dependence can explain the variability of ^{10}Be inventories in some soil profiles (Dixon et al., 2018; Graly et al., 2011). Other studies, however, have observed no correlation between soil-derived ^{10}Be flux and precipitation rates (Ouimet et al., 2015; Willenbring and von Blanckenburg, 2010). For the studied terraces we observed no clear correlation between precipitation rate and depositional flux (Table 3 and Fig. 9). Unless such correlation is obliterated by compounding effects the difference in ^{10}Be delivery should be secondary between sampling locations. We thus consider that the difference in depositional fluxes derived from the three terraces should be minor. As such, the overlapping range of all the terrace-derived flux estimates (Fig. 9) is considered as the first-order flux estimate for the Taiwan orogen, that is, $0.66\text{-}0.88 \times 10^6 \text{ at/cm}^2/\text{yr}$.

When comparing to other two approaches, the plausible range of terrace-derived fluxes is consistently lower. Specifically, the flux from rainfall data fitting in each sampling location can be even 3-4 times higher than the upper-bound limit of terrace-derived flux (Fig. 9) and is thus unlikely to be realistic in the study area. In comparison, the GCM-derived flux is closer to but still higher than the corresponding terrace-derived flux (Fig. 9). Such flux offset may be partly explained by the uncertainty in ^{10}Be production models implemented in the GCM. For example, the production model adopted by the GCM applied here (Heikkilä and von Blanckenburg, 2015) gives a global average ^{10}Be production rate of $0.21 \text{ at/cm}^2/\text{yr}$ (Masarik and Beer, 2009), while other rate estimates using different production models can vary from e.g. $0.19 \text{ at/cm}^2/\text{yr}$ (Webber et al., 2007) to $0.32 \text{ at/cm}^2/\text{yr}$ (Kovaltsov and Usoskin, 2010). Furthermore, such comparison shown for the Taiwan orogen is consistent with that revealed by the recent compilation of global ^{10}Be depositional fluxes from multiple approaches,

indicating that a realistic flux commonly stays between measured soil-derived fluxes and GCM-derived fluxes (Deng et al., 2020a).

5.4. Implications for the precipitation effect in the Taiwan orogen

The site-specific calibration in this study provides further implications for the precipitation effect on ^{10}Be depositional flux. To account for the existing conflicting views on the presence of the precipitation effect as mentioned above, Willenbring and von Blanckenburg (2010) proposed two ^{10}Be delivery effects, i.e. the dilution effect and the additive effect. ^{10}Be concentrations in rain are assumed to be constant in the additive effect and thus the ^{10}Be depositional flux depends on precipitation rate. The rainfall-based fitting equation (Graly et al., 2011) is derived assuming a sole additive effect. However, in the dilution effect, ^{10}Be contained in proximal rain sources is mainly limited by the ^{10}Be flux at which it is introduced into the lower atmosphere and thus the depositional flux is independent of precipitation rate (Willenbring and von Blanckenburg, 2010). Both effects can also exist in combination at a certain geographical setting such as orogens.

In the Taiwan orogen, the realistic Holocene ^{10}Be depositional flux we estimated is much lower (<50%) than the flux derived from rainfall data fitting. This result suggests a potential overestimation of the control of precipitation by this fitting equation due to underestimation of the precipitation dilution effect. We thus conclude that in the Taiwan orogen, ^{10}Be depositional flux does not increase proportionally with precipitation rate and the dilution effect may play a major role in millennial-scale ^{10}Be deposition here. This new piece of evidence also fits in with the recent global compilation of ^{10}Be fluxes: the short-term rainfall-derived flux commonly exceeds the millennial-scale soil-derived estimate, as short-term stochasticity in precipitation events could introduce a measurement time-interval bias towards higher fluxes (Deng et al., 2020a).

6. Conclusions

We measured ^{10}Be and ^9Be concentrations in three river terraces of Taiwan Island, in order to quantify deposition and retention processes of meteoric ^{10}Be in Holocene archives. Compared to previous efforts on estimation of the long-term ^{10}Be depositional flux (Clow et al., 2020; Dixon et al., 2018; Ouimet et al., 2015; Reusser et al., 2010), the terraces of this study have the deepest sampling depths (e.g. 5.8-6.2 m) and youngest ages (<10 ka). This new dataset explicitly evaluates controls of vertical migration of Be isotopes in young soil profiles, and provides further constraints on long-term ^{10}Be depositional flux in the Taiwan orogen. The main conclusions are as follows:

1) The millennial-scale ^{10}Be depositional flux derived from ^{10}Be inventory of each terrace, corrected for ^{10}Be inheritance only, ranges from 0.32 to 0.49×10^6 at/cm²/yr. However, we regard this flux as a lower-bound estimate, because potential presence of low Be retentivity, surface erosion, multi-phase sediment deposition and incomplete sampling depth can cause violation of assumptions on calculating terrace-derived ^{10}Be fluxes.

2) We quantitatively evaluate the effect of each scenario above on the ^{10}Be depositional flux and further provide a plausible range of flux estimates for each terrace. The overlapping range of flux estimates from all the terraces is $0.66\text{-}0.88 \times 10^6$ at/cm²/yr.

3) We compare this newly constrained range of terrace-derived fluxes with independent flux estimates from GCM (Heikkilä and von Blanckenburg, 2015) and from a rainfall-based fitting equation (Graly et al., 2011). The flux from rainfall data fitting is >2 times higher than our terrace-derived flux, indicating an overestimation of the control of precipitation in the Taiwan orogen. In comparison, the GCM-derived flux is closer to but still overestimates the millennial-scale ^{10}Be depositional flux by at least 23%.

In summary, we recommend to use a range of terrace-derived fluxes obtained in this study ($0.66-0.88 \times 10^6$ at/cm²/yr) for Earth surface applications in the fast-eroding Taiwan orogen, especially in regions with similar climatic conditions (precipitation rate of 2-3 m/yr) as the studied terraces.

Appendix A. Conceptual framework on estimation of ¹⁰Be desorption loss

To estimate the desorption loss of Be due to low soil pH, we here develop a partition coefficient (K_d)-based method. Taking the soil column as a whole and assuming a constant pH with time, the change in ¹⁰Be inventory at a given time (t) is the deposition of meteoric ¹⁰Be from the surface minus the removal of ¹⁰Be from the soil column due to desorption:

$$\frac{dI_{10}(t)}{dt} = F_{\text{met}} - \frac{Q}{MK_d} I_{10}(t) \quad (\text{A.1})$$

where Q is the runoff through the soil profile (m/yr) and M the total mass of the soil column (kg/m²) that is assumed not to change with time. To calculate Q, we use a published empirical relationship between precipitation rate and runoff in Taiwan, where $Q = -0.025 \times P^2 + 0.820 \times P$ (P is precipitation rate, in m/yr) (Deng et al., 2020b). Here modern precipitation rates (Table 3) are adopted for this calculation. The variability in precipitation rate may be minor during the study period because the Taiwan orogen is dominated by subtropical-wet climate consistently during the Holocene (Liew et al., 2006). To obtain the pH-dependent K_d , we apply a published empirical fitting equation that relates soil pH (in H₂O) and K_d mainly based on sorption experimental data using clays and silt/sand, that is, $K_d = 10^{5.82/(1+\exp(-(1.82+0.55 \times \text{pH})))}$ (Campforts et al., 2016).

After integrating Eq. (A.1) from the terrace depositional age (t) to present-day, the time-integrated ¹⁰Be inventory ($I_{10,t}$) accounting for desorption loss is:

$$I_{10,t} = \frac{F_{\text{met}} - e^{\frac{-Qt}{MK_d}} \left(F_{\text{met}} - \frac{Q}{MK_d} I_{10,inh} \right)}{\frac{Q}{MK_d}} \quad (\text{A.2})$$

where $I_{10,inh}$ is the initial inventory of ^{10}Be at the time of terrace deposition inherited from the previous erosion process. The ratio of $I_{10,t}$ to a theoretical inventory assuming full retention of ^{10}Be will derive the theoretical fractional loss of ^{10}Be inventory caused by desorption ($I_{10,loss}$) after subtracted from 100%:

$$I_{10,loss} = 1 - \frac{F_{met} - e^{\frac{-Qt}{MK_d}} \times (F_{met} - \frac{Q}{MK_d} I_{10,inh})}{\frac{Q}{MK_d} (F_{met} t + I_{10,inh})} \quad (\text{A.3})$$

We thus use Eq. (A.3) to correct for desorption loss of ^{10}Be inventory in Section 5.2. Please note that $I_{10,loss}$ is relatively insensitive to the non-prior-known F_{met} , and shifts by less than 10% for varying F_{met} by one order of magnitude (see [Supplementary materials](#)).

Appendix B. Calculation of denudation rates using ^{10}Be (meteoric)/ ^9Be ratios

To calculate denudation rates using Be isotopic data in terrace sediments unaffected by post-depositional alteration, we adopt the steady-state mass balance framework for the ^{10}Be (meteoric)/ ^9Be system developed by [von Blanckenburg et al. \(2012\)](#). The ^{10}Be (meteoric)/ ^9Be -derived denudation rate (D_{met} , in $\text{kg}/\text{m}^2/\text{yr}$, or in mm/yr when using a density of $2.65 \times 10^3 \text{ kg}/\text{m}^3$ for conversion) can be calculated using a simplified equation:

$$D_{met} = \frac{F_{met}}{\left(\frac{^{10}\text{Be}}{^9\text{Be}}\right)_{\text{reac}} \times \left[\frac{^9\text{Be}}{^9\text{Be}}\right]_{\text{parent}}} \times \left(\left[\frac{^9\text{Be}}{^9\text{Be}}\right]_{\text{min}} + 1\right) \quad (\text{B.1})$$

where $[^9\text{Be}]_{\text{parent}}$ (mg/kg) is the ^9Be concentration of the parent bedrock prior to weathering. For terrace XX we use the same parameterization as that used for the modern Chenyoulan River by [Deng et al. \(2020b\)](#), including a $[^9\text{Be}]_{\text{parent}}$ of $2.03 \pm 0.37 \text{ } \mu\text{g}/\text{g}$ and GCM-derived F_{met} of $1.08 \pm 0.03 \times 10^6 \text{ at}/\text{cm}^2/\text{yr}$. The bottom three sampled layers are used for denudation rate calculation, with an average $(^{10}\text{Be}/^9\text{Be})_{\text{reac}}$ of 1.67×10^{-10} . The detailed derivation for Eq. (B.1) including requirements and assumptions is given in [von Blanckenburg et al. \(2012\)](#).

587

588 **Acknowledgements**

589 We thank Quentin Simon and one anonymous reviewer for their valuable comments. We gratefully
590 acknowledge the valuable discussions with Benjamin Campforts and Veerle Vanacker. We thank Yuan-
591 Pin Chang and Chenyu Wang for their help during the field trip to Taiwan Island and Steve Binnie and
592 Stefan Heinze from Cologne University for providing AMS measurements. KD and SY thank the
593 support by the National Natural Science Foundation of China (Grant No. 42006059, 41991324 and
594 41730531). KD also thanks the Freie Universität Berlin-China Scholarship Council (FUB-CSC) PhD
595 Program for his scholarship in Germany.

596

597 **References:**

- 598 Bacon, A.R., Richter, D.d., Bierman, P.R., Rood, D.H., 2012. Coupling meteoric ^{10}Be with pedogenic
599 losses of ^9Be to improve soil residence time estimates on an ancient North American interfluvium.
600 *Geology* 40, 847-850.
- 601 Bierman, P.R., Caffee, M.W., Davis, P.T., Marsella, K., Pavich, M., Colgan, P., Mickelson, D., Larsen,
602 J., 2002. Rates and timing of earth surface processes from in situ-produced cosmogenic Be-10 . *Rev.*
603 *Mineral. Geochem.* 50, 147-205.
- 604 Campforts, B., Vanacker, V., Vanderborght, J., Baken, S., Smolders, E., Govers, G., 2016. Simulating
605 the mobility of meteoric ^{10}Be in the landscape through a coupled soil-hillslope model (Be2D).
606 *Earth Planet. Sci. Lett.* 439, 143-157.
- 607 Ching, K.-E., Hsieh, M.-L., Johnson, K.M., Chen, K.-H., Rau, R.-J., Yang, M., 2011. Modern vertical
608 deformation rates and mountain building in Taiwan from precise leveling and continuous GPS
609 observations, 2000-2008. *Journal of Geophysical Research-Solid Earth* 116, 1-16.

610 Chmeleff, J., von Blanckenburg, F., Kossert, K., Jakob, D., 2010. Determination of the ^{10}Be half-life
611 by multicollector ICP-MS and liquid scintillation counting. *Nucl. Instrum. Methods Phys. Res.,*
612 *Sect. B* 268, 192-199.

613 Clow, T., Willenbring, J.K., Schaller, M., Blum, J.D., Christl, M., Kubik, P.W., von Blanckenburg, F.,
614 2020. Calibrating a long-term meteoric ^{10}Be delivery rate into eroding western US glacial deposits
615 by comparing meteoric and in situ produced ^{10}Be depth profiles. *Geochronology* 2, 411-423.

616 Cook, K.L., Turowski, J.M., Hovius, N., 2014. River gorge eradication by downstream sweep erosion.
617 *Nature Geosci* 7, 682-686.

618 Dadson, S.J., Hovius, N., Chen, H.G., Dade, W.B., Hsieh, M.L., Willett, S.D., Hu, J.C., Horng, M.J.,
619 Chen, M.C., Stark, C.P., Lague, D., Lin, J.C., 2003. Links between erosion, runoff variability and
620 seismicity in the Taiwan orogen. *Nature* 426, 648-651.

621 Deng, K., Wittmann, H., von Blanckenburg, F., 2020a. The depositional flux of meteoric cosmogenic
622 ^{10}Be from modeling and observation. *Earth Planet. Sci. Lett.* 550, 116530.

623 Deng, K., Yang, S., von Blanckenburg, F., Wittmann, H., 2020b. Denudation Rate Changes Along a
624 Fast-Eroding Mountainous River With Slate Headwaters in Taiwan From ^{10}Be (Meteoric)/ ^9Be
625 Ratios. *Journal of Geophysical Research: Earth Surface* 125, e2019JF005251.

626 Derriex, F., Siame, L.L., Bourlès, D.L., Chen, R.F., Braucher, R., Léanni, L., Lee, J.C., Chu, H.T.,
627 Byrne, T.B., 2014. How fast is the denudation of the Taiwan mountain belt? Perspectives from in
628 situ cosmogenic ^{10}Be . *J. Asian Earth Sci.* 88, 230-245.

629 Dixon, J.L., Chadwick, O.A., Pavich, M.J., 2018. Climatically controlled delivery and retention of
630 meteoric ^{10}Be in soils. *Geology* 46, 899-902.

631 Egli, M., Brandová, D., Böhlert, R., Favilli, F., Kubik, P.W., 2010. ^{10}Be inventories in Alpine soils and
632 their potential for dating land surfaces. *Geomorphology* 119, 62-73.

633 Fick, S.E., Hijmans, R.J., 2017. WorldClim 2: new 1-km spatial resolution climate surfaces for global
634 land areas. *Int. J. Climatol.* 37, 4302-4315.

635 Field, C.V., Schmidt, G.A., Koch, D., Salyk, C., 2006. Modeling production and climate-related impacts
636 on Be-10 concentration in ice cores. *Journal of Geophysical Research-Atmospheres* 111, 1-13.

637 Graham, I., Ditchburn, R., Barry, B., 2003. Atmospheric deposition of ^7Be and ^{10}Be in New Zealand
638 rain (1996-98). *Geochim. Cosmochim. Acta* 67, 361-373.

639 Graly, J.A., Bierman, P.R., Reusser, L.J., Pavich, M.J., 2010. Meteoric ^{10}Be in soil profiles – A global
640 meta-analysis. *Geochim. Cosmochim. Acta* 74, 6814-6829.

641 Graly, J.A., Reusser, L.J., Bierman, P.R., 2011. Short and long-term delivery rates of meteoric ^{10}Be to
642 terrestrial soils. *Earth Planet. Sci. Lett.* 302, 329-336.

643 Granger, D.E., Schaller, M., 2014. Cosmogenic Nuclides and Erosion at the Watershed Scale. *Elements*
644 10, 369-373.

645 Hartshorn, K., Hovius, N., Dade, W.B., Slingerland, R.L., 2002. Climate-driven bedrock incision in an
646 active mountain belt. *Science* 297, 2036-2038.

647 Heikkilä, U., Beer, J., Abreu, J.A., Steinhilber, F., 2013a. On the Atmospheric Transport and Deposition
648 of the Cosmogenic Radionuclides (^{10}Be): A Review. *Space Sci. Rev.* 176, 321-332.

649 Heikkilä, U., Phipps, S.J., Smith, A.M., 2013b. Be-10 in late deglacial climate simulated by ECHAM5-
650 HAM - Part 1: Climatological influences on Be-10 deposition. *Clim. Past* 9, 2641-2649.

651 Heikkilä, U., von Blanckenburg, F., 2015. The global distribution of Holocene meteoric ^{10}Be fluxes
652 from atmospheric models. Distribution maps for terrestrial Earths surface applications, GFZ Data
653 Services, GFZ Potsdam, Germany.

654 Hilton, R.G., Galy, A., Hovius, N., Chen, M.-C., Horng, M.-J., Chen, H., 2008. Tropical-cyclone-driven
 655 erosion of the terrestrial biosphere from mountains. *Nature Geosci* 1, 759-762.

656 Hovius, N., Lin, J.C., 2000. Supply and Removal of Sediment in a Landslide-Dominated Mountain
 657 Belt: Central Range, Taiwan. *J. Geol.* 108, 73-89.

658 Hovius, N., Meunier, P., Lin, C.-W., Chen, H., Chen, Y.-G., Dadson, S., Horng, M.-J., Lines, M., 2011.
 659 Prolonged seismically induced erosion and the mass balance of a large earthquake. *Earth Planet.*
 660 *Sci. Lett.* 304, 347-355.

661 Hsieh, M.-L., Capart, H., 2013. Late Holocene episodic river aggradation along the Lao-nong River
 662 (southwestern Taiwan): An application to the Tseng-wen Reservoir Transbasin Diversion Project.
 663 *Eng. Geol.* 159, 83-97.

664 Hsieh, M.-L., Chyi, S.-J., 2010. Late Quaternary mass-wasting records and formation of fan terraces in
 665 the Chen-yeo-lan and Lao-nung catchments, central-southern Taiwan. *Quat. Sci. Rev.* 29, 1399-
 666 1418.

667 Hsieh, M.-L., Hogg, A., Song, S.-R., Kang, S.-C., Chou, C.-Y., 2017. A mass-wasting dominated
 668 Quaternary mountain range, the Coastal Range in eastern Taiwan. *Quat. Sci. Rev.* 177, 276-298.

669 Hsieh, M.-L., Liew, P.-M., Chen, H.-W., 2011. Early Holocene catastrophic mass-wasting event and
 670 fan-delta development on the Hua-tung coast, eastern Taiwan. *Geomorphology* 134, 378-393.

671 Hsu, W.-H., Byrne, T.B., Ouimet, W., Lee, Y.-H., Chen, Y.-G., Soest, M.v., Hodges, K., 2016.
 672 Pleistocene onset of rapid, punctuated exhumation in the eastern Central Range of the Taiwan
 673 orogenic belt. *Geology* 44, 719-722.

674 Huang, C.Y., Yuan, P.B., Tsao, S.J., 2006. Temporal and spatial records of active arc-continent
 675 collision in Taiwan: A synthesis. *Geol. Soc. Am. Bull.* 118, 274-288.

676 Jelinski, N.A., Campforts, B., Willenbring, J.K., Schumacher, T.E., Li, S., Lobb, D.A., Papiernik, S.K.,
 677 Yoo, K., 2019. Meteoric Beryllium-10 as a tracer of erosion due to post-settlement land use in west-
 678 central Minnesota, USA. *Journal of Geophysical Research: Earth Surface* 124, 874-901.

679 Johnson, M.O., Mudd, S.M., Pillans, B., Spooner, N.A., Keith Fifield, L., Kirkby, M.J., Gloor, M.,
 680 2014. Quantifying the rate and depth dependence of bioturbation based on optically-stimulated
 681 luminescence (OSL) dates and meteoric ^{10}Be . *Earth Surf. Processes Landforms* 39, 1188-1196.

682 Jungers, M.C., Bierman, P.R., Matmon, A., Nichols, K., Larsen, J., Finkel, R., 2009. Tracing hillslope
 683 sediment production and transport with in situ and meteoric ^{10}Be . *Journal of Geophysical*
 684 *Research: Earth Surface* 114.

685 Kao, S.J., Milliman, J.D., 2008. Water and Sediment Discharge from Small Mountainous Rivers,
 686 Taiwan: The Roles of Lithology, Episodic Events, and Human Activities. *J. Geol.* 116, 431-448.

687 Korschinek, G., Bergmaier, A., Faestermann, T., Gerstmann, U.C., Knie, K., Rugel, G., Wallner, A.,
 688 Dillmann, I., Dollinger, G., Gostonski, C.L.V., 2010. A new value for the half-life of ^{10}Be by
 689 Heavy-Ion Elastic Recoil Detection and liquid scintillation counting. *Nuclear Instruments &*
 690 *Methods in Physics Research* 268, 187-191.

691 Kovaltsov, G.A., Usoskin, I.G., 2010. A new 3D numerical model of cosmogenic nuclide ^{10}Be
 692 production in the atmosphere. *Earth Planet. Sci. Lett.* 291, 182-188.

693 Lal, D., 1991. Cosmic ray labeling of erosion surfaces: in situ nuclide production rates and erosion
 694 models. *Earth Planet. Sci. Lett.* 104, 424-439.

695 Lee, Y.H., Chen, C.C., Liu, T.K., Ho, H.C., Lu, H.Y., Wei, L., 2006. Mountain building mechanisms
 696 in the Southern Central Range of the Taiwan Orogenic Belt — From accretionary wedge
 697 deformation to arc–continental collision. *Earth Planet. Sci. Lett.* 252, 413-422.

698 Liew, P.-M., Huang, S.-Y., Kuo, C.-M., 2006. Pollen stratigraphy, vegetation and environment of the
699 last glacial and Holocene—A record from Toushe Basin, central Taiwan. *Quat. Int.* 147, 16-33.

700 Maher, K., von Blanckenburg, F., 2016. Surface ages and weathering rates from ^{10}Be (meteoric) and
701 $^{10}\text{Be}/^9\text{Be}$: Insights from differential mass balance and reactive transport modeling. *Chem. Geol.*
702 446, 70-86.

703 Masarik, J., Beer, J., 2009. An updated simulation of particle fluxes and cosmogenic nuclide production
704 in the Earth's atmosphere. *Journal of Geophysical Research: Atmospheres* 114, 1-9.

705 Mckean, J.A., Dietrich, W.E., Finkel, R.C., Southon, J.R., Caffee, M.W., 1993. Quantification of soil
706 production and downslope creep rates from cosmogenic ^{10}Be accumulations on a hillslope profile.
707 *Geology* 21, 343-346.

708 Milliman, J.D., Farnsworth, K.L., 2011. *River Discharge to the Coastal Ocean – A Global Synthesis.*
709 Cambridge University Press.

710 Monaghan, M.C., Krishnaswami, S., Turekian, K.K., 1986. The global-average production rate of 10
711 Be . *Earth Planet. Sci. Lett.* 76, 279-287.

712 Ouimet, W., Dethier, D., Bierman, P., Wyshnytzky, C., Shea, N., Rood, D.H., 2015. Spatial and
713 temporal variations in meteoric ^{10}Be inventories and long-term deposition rates, Colorado Front
714 Range. *Quat. Sci. Rev.* 109, 1-12.

715 Pavich, M.J., Brown, L., Harden, J., Klein, J., Middleton, R., 1986. ^{10}Be distribution in soils from
716 Merced River terraces, California. *Geochim. Cosmochim. Acta* 50, 1727-1735.

717 Reusser, L., Graly, J., Bierman, P., Rood, D., 2010. Calibrating a long-term meteoric ^{10}Be
718 accumulation rate in soil. *Geophys. Res. Lett.* 37.

719 Schoonejans, J., Vanacker, V., Opfergelt, S., Christl, M., 2017. Long-term soil erosion derived from in-
720 situ ^{10}Be and inventories of meteoric ^{10}Be in deeply weathered soils in southern Brazil. *Chem.*
721 *Geol.*

722 Siame, L.L., Chen, R.F., Derrieux, F., Lee, J.C., Chang, K.J., Bourlès, D.L., Braucher, R., Léanni, L.,
723 Kang, C.C., Chang, C.P., 2012. Pleistocene alluvial deposits dating along frontal thrust of
724 Changhua Fault in western Taiwan: The cosmic ray exposure point of view. *J. Asian Earth Sci.* 51,
725 1-20.

726 Simon, Q., Thouveny, N., Bourlès, D.L., Nuttin, L., Hillaire-Marcel, C., St-Onge, G., 2016. Authigenic
727 $^{10}\text{Be}/^{9}\text{Be}$ ratios and ^{10}Be -fluxes (^{230}Th xs -normalized) in central Baffin Bay sediments during
728 the last glacial cycle: Paleoenvironmental implications. *Quat. Sci. Rev.* 140, 142-162.

729 Steinhilber, F., Abreu, J.A., Beer, J., Brunner, I., Christl, M., Fischer, H., Heikkilä, U., Kubik, P.W.,
730 Mann, M., McCracken, K.G., Miller, H., Miyahara, H., Oerter, H., Wilhelms, F., 2012. 9,400 years
731 of cosmic radiation and solar activity from ice cores and tree rings. *Proceedings of the National*
732 *Academy of Sciences* 109, 5967-5971.

733 Uhlig, D., Amelung, W., von Blanckenburg, F., 2020. Mineral Nutrients Sourced in Deep Regolith
734 Sustain Long-Term Nutrition of Mountainous Temperate Forest Ecosystems. *Global Biogeochem.*
735 *Cycles* 34, e2019GB006513.

736 von Blanckenburg, F., Belshaw, N.S., O'Nions, R.K., 1996. Separation of ^9Be and cosmogenic ^{10}Be
737 from environmental materials and SIMS isotope dilution analysis. *Chem. Geol.* 129, 93-99.

738 von Blanckenburg, F., Bouchez, J., Wittmann, H., 2012. Earth surface erosion and weathering from the
739 Be-10 (meteoric)/ Be-9 ratio. *Earth Planet. Sci. Lett.* 351, 295-305.

740 von Blanckenburg, F., Willenbring, J.K., 2014. Cosmogenic Nuclides: Dates and Rates of Earth-Surface
741 Change. *Elements* 10, 341-346.

742 Webber, W.R., Higbie, P.R., McCracken, K.G., 2007. Production of the cosmogenic isotopes ^3H , ^7Be ,
743 ^{10}Be , and ^{36}Cl in the Earth's atmosphere by solar and galactic cosmic rays. *Journal of Geophysical*
744 *Research: Space Physics* 112.

745 Willenbring, J.K., von Blanckenburg, F., 2010. Meteoric cosmogenic Beryllium-10 adsorbed to river
746 sediment and soil: Applications for Earth-surface dynamics. *Earth Sci. Rev.* 98, 105-122.

747 Wittmann, H., von Blanckenburg, F., Bouchez, J., Dannhaus, N., Naumann, R., Christl, M., Gaillardet,
748 J., 2012. The dependence of meteoric Be-10 concentrations on particle size in Amazon River bed
749 sediment and the extraction of reactive Be-10/Be-9 ratios. *Chem. Geol.* 318, 126-138.

750 You, C.F., Lee, T., Li, Y.H., 1989. The partition of Be between soil and water. *Chem. Geol.* 77, 105-
751 118.

752

753 **Table 1** Basic properties of sampled terrace sediments.

Sample	Depth m	Density ¹ g/cm ³	pH ²	<2 mm volume ³ %
Xinxiang terrace (XX)				
Location: 23.6534 °N, 120.8743 °E				
XX-1-1	0.00	0.86	4.34	92.4%
XX-1-4	0.00	0.86	4.83	92.4%
XX1-5	0.20	1.04	3.85	86.9%
XX2	0.45	1.04	3.88	84.8%
XX3	0.80	1.04	3.94	82.8%
XX4	1.15	1.04	4.49	76.8%
XX6	2.20	1.04	5.44	79.4%
XX7	3.10	1.04	5.65	67.9%
XX8	4.70	1.04	6.07	71.9%
XX10	6.20	1.04	6.09	79.1%
Shengguang terrace (SG)				
Location: 24.3705 °N, 121.3390 °E				
SG1-1	0.00	0.76	7.02	85.0%
SG1-4	0.00	0.76	6.99	85.0%
SG2	0.25	0.76	6.71	86.3%
SG3	0.40	1.71	6.26	62.6%
SG4	0.55	1.71	5.51	52.0%
SG5	1.00	1.71	3.85	59.4%
SG6	1.50	1.71	3.92	56.5%
SG8	2.35	1.71	4.36	46.5%
SG9	3.20	1.71	4.91	54.4%
Changbin terrace (CB)⁴				
Location: 23.3193 °N, 121.4545 °E				
CB-surface	0.00	1.32	5.84	100.0%
CB1C	0.00	1.32	6.02	100.0%
CB2C	0.22	1.87	6.37	84.4%
CB3C	0.51	1.87	6.49	67.2%
CB4C	0.82	1.87	6.44	87.5%
CB5C	1.22	1.87	6.46	89.7%
CB6C	1.63	1.87	6.48	98.9%
CB8C	2.66	1.87	5.60	99.4%
CB12C	5.88	1.87	7.00	86.1%

754

755 Note: 1) To obtain the bulk density, three samples were collected with a known volume from top,
756 middle, and bottom, respectively; after oven-drying, the samples were weighed. The bulk density of
757 the surface layer is measured including a relative error of 10%. To assign a density value to each
758 subsurface terrace layer, we use the average value of the two density measurements taken below the
759 surface as bulk density, including an error of the standard deviation of both measurements.

760 2) Soil pH was determined on the sieved < 2 mm fraction of air-dried samples using a soil-solution
761 (0.01 M CaCl₂) ratio of 1:2.

762 3) To calculate the <2 mm volume, we separate the coarse fraction (> 2 mm) of each terrace layer into
763 two parts and determine each in different approaches. ① The >2 mm fraction contained in the
764 collected samples. The weight percentage of this fraction is determined by sieving (using a 2 mm
765 sieve) and weighing and was then converted to volumetric percentage. ② The unsampled boulders in
766 the profile. Given their large size (a diameter of > 6 cm in our case), we manually extracted their areal
767 percentage from the photos of each profile and convert areal percentage to volumetric percentage. The
768 <2 mm volume is then calculated using Eq. (2).

769 4) No preserved outcrops of terrace CB were found in the field, and thus a sediment core was drilled
770 from the surface ([Hsieh et al., 2017](#)).

771

Table 2 Concentrations of meteoric ^{10}Be and stable ^9Be in reactive (reac) and silicate residual (min) fractions.

Sample ^{1,2,3}	$[^9\text{Be}]_{\text{reac}}$ $\mu\text{g/g}$	$[^9\text{Be}]_{\text{min}}$ $\mu\text{g/g}$	$[^{10}\text{Be}]_{\text{reac}}^4$ $\times 10^6 \text{ at/g}$	$[^{10}\text{Be}]_{\text{min}}^4$ $\times 10^6 \text{ at/g}$	$f_{\text{reac-10}}^5$ %
Xinxiang terrace (XX)					
XX-1-1*	0.39 ± 0.02	0.66 ± 0.03	40.56 ± 1.45	9.13 ± 0.53	81.6%
XX-1-4	0.38 ± 0.02	0.65 ± 0.03	33.41 ± 1.22		
XX1-5*	0.41 ± 0.02	0.81 ± 0.04	34.19 ± 1.25		
XX2	0.49 ± 0.02	0.89 ± 0.04	31.16 ± 1.15		
XX3	0.82 ± 0.04	1.15 ± 0.06	19.84 ± 0.78		
XX4*	0.70 ± 0.03	1.18 ± 0.06	10.12 ± 0.50		
XX6*	0.74 ± 0.04	1.15 ± 0.06	10.41 ± 0.51		
XX7	0.62 ± 0.03	1.14 ± 0.06	6.50 ± 0.35		
XX8	0.66 ± 0.03	1.09 ± 0.05	7.09 ± 0.38		
XX10*	0.59 ± 0.03	1.14 ± 0.06	7.19 ± 0.38	2.49 ± 0.29	74.3%
Shengguang terrace (SG)					
SG1-1	0.65 ± 0.03	0.89 ± 0.04	24.85 ± 1.04		
SG1-4	0.58 ± 0.03	0.99 ± 0.05	21.67 ± 1.15		
SG2*	0.75 ± 0.04	1.45 ± 0.07	21.69 ± 0.85	3.55 ± 0.35	85.9%
SG3	0.61 ± 0.03	1.63 ± 0.08	2.93 ± 0.23		
SG4*	0.67 ± 0.03	1.73 ± 0.09	1.59 ± 0.16		
SG5	0.71 ± 0.04	1.81 ± 0.09	1.57 ± 0.16		
SG6*	0.74 ± 0.04	1.88 ± 0.09	3.02 ± 0.22		
SG8	1.07 ± 0.05	2.07 ± 0.10	4.48 ± 0.28		
SG9*	0.84 ± 0.04	2.01 ± 0.10	7.64 ± 0.39	3.10 ± 0.30	71.1%
Changbin terrace (CB)					
CB-surface	0.29 ± 0.01	0.22 ± 0.01	68.34 ± 2.29		
CB1C*	0.27 ± 0.01	0.23 ± 0.01	65.26 ± 2.22	12.52 ± 0.68	83.9%
CB2C*	0.17 ± 0.01	0.25 ± 0.01	12.18 ± 0.57		
CB3C	0.17 ± 0.01	0.42 ± 0.02	9.29 ± 0.46		
CB4C*	0.15 ± 0.01	0.27 ± 0.01	5.87 ± 0.37		
CB5C	0.15 ± 0.01	0.23 ± 0.01	3.22 ± 0.24		
CB6C*	0.13 ± 0.01	0.20 ± 0.01	0.87 ± 0.12		
CB8C	0.11 ± 0.01	0.20 ± 0.01	0.98 ± 0.12		
CB12C*	0.12 ± 0.01	0.27 ± 0.01	0.47 ± 0.09	0.60 ± 0.20	44.3%

Note: 1) The order of samples is the same as Table 1.

2) All uncertainties denote 1σ analytical error. For ^9Be measurements using ICP-OES, the given uncertainty (5%) is the long-term repeatability.

3) All samples were processed in two batches, and the samples with an asterisk belong to the first batch.

4) We use a blank $^{10}\text{Be}/^9\text{Be}$ ratio of $0.74 \pm 0.21 \times 10^{-15}$ ($n=2$) and $8.32 \pm 1.30 \times 10^{-15}$ ($n=1$) to perform the blank correction for reactive (reac) fractions and residual (min) fractions, respectively.

5) $f_{\text{reac-10}}$ is the proportion of reactive ^{10}Be relative to bulk ^{10}Be (sum of reac and min fractions).

782 **Table 3** Terrace-derived ^{10}Be inventories and calculated depositional fluxes.

783

Terrace	Depositional age ¹	Rainfall ²	^{10}Be reactivity inventory ³	Inherited ^{10}Be reactivity ⁴	Total corrected ^{10}Be inventory ⁵	Measured ^{10}Be depositional flux	Proposed upper flux limit ⁶
	ka	m/yr	$\times 10^9$ at/cm ²	$\times 10^6$ at/g	$\times 10^9$ at/cm ²	$\times 10^6$ at/cm ² /yr	$\times 10^6$ at/cm ² /yr
XX	9.05 ± 0.35	2.46	6.10 ± 0.21	6.97 ± 0.37	2.91 ± 0.15	0.32 ± 0.02	0.94-2.26
SG	3.83 ± 0.36	2.89	1.74 ± 0.08	0.81 ± 0.13	1.89 ± 0.10	0.49 ± 0.05	0.80-0.88
CB	7.07 ± 0.89	2.08	3.10 ± 0.20	0.47 ± 0.09	3.20 ± 0.23	0.45 ± 0.07	0.80-0.93

784

785 Note: 1) The ^{14}C ages of terraces XX and CB, calibrated in years before present (cal. BP), are from [Hsieh and Chyi \(2010\)](#) and [Hsieh et al. \(2017\)](#).

786 2) The rainfall data is sourced from WorldClim Version2 ([Fick and Hijmans, 2017](#)).

787 3) ^{10}Be reactivity inventory is the inventory derived from ^{10}Be reactivity summed over the sampled depth of each terrace without correction for inheritance.

788 4) Inherited ^{10}Be reactivity is derived from soil mass-weighted ^{10}Be reactivity of the bottom three samples for XX, from the ^{10}Be reactivity in the headwaters of the Zhuoshui
789 River nearby for SG (ZS-1 in [Fig. 1](#), [Deng et al. \(2020b\)](#)), and from the ^{10}Be reactivity of the bottom-most sample for CB. The proposed inherited ^{10}Be reactivity (0.81×10^6
790 at/g) in terrace SG is much lower than ^{10}Be reactivity of the bottom sample (7.64×10^6 at/g). We consider that the latter is affected by contribution of dissolved ^{10}Be
791 delivered from depths above.

792 5) Inventory corrected for inherited ^{10}Be and converted to a bulk ^{10}Be inventory using an average percentage of reactive ^{10}Be of 78.2%.

793 6) Details on constraining this upper limit of ^{10}Be depositional flux is provided in Section 5.2.

794

795

796

797

798

Table 4

Scenarios on violation of assumptions on ¹⁰Be flux derivation and their parameterization.

Terrace	Violation of assumptions ¹			
	Low Be retentivity	Surface erosion	Multi-phase deposition	Incomplete sampling
XX	pH: 3.85-4.62	×	Age < 9.05 ka	×
SG	pH: 4.68-7.02	×	×	Unsampled depth > 0 m
CB	×	Rate > 0 cm/yr	×	×

Note: 1) “×” indicates that the corresponding assumption is considered to be valid in a terrace. The parameterization of each scenario is explained in Sections 5.2.1-5.2.3.

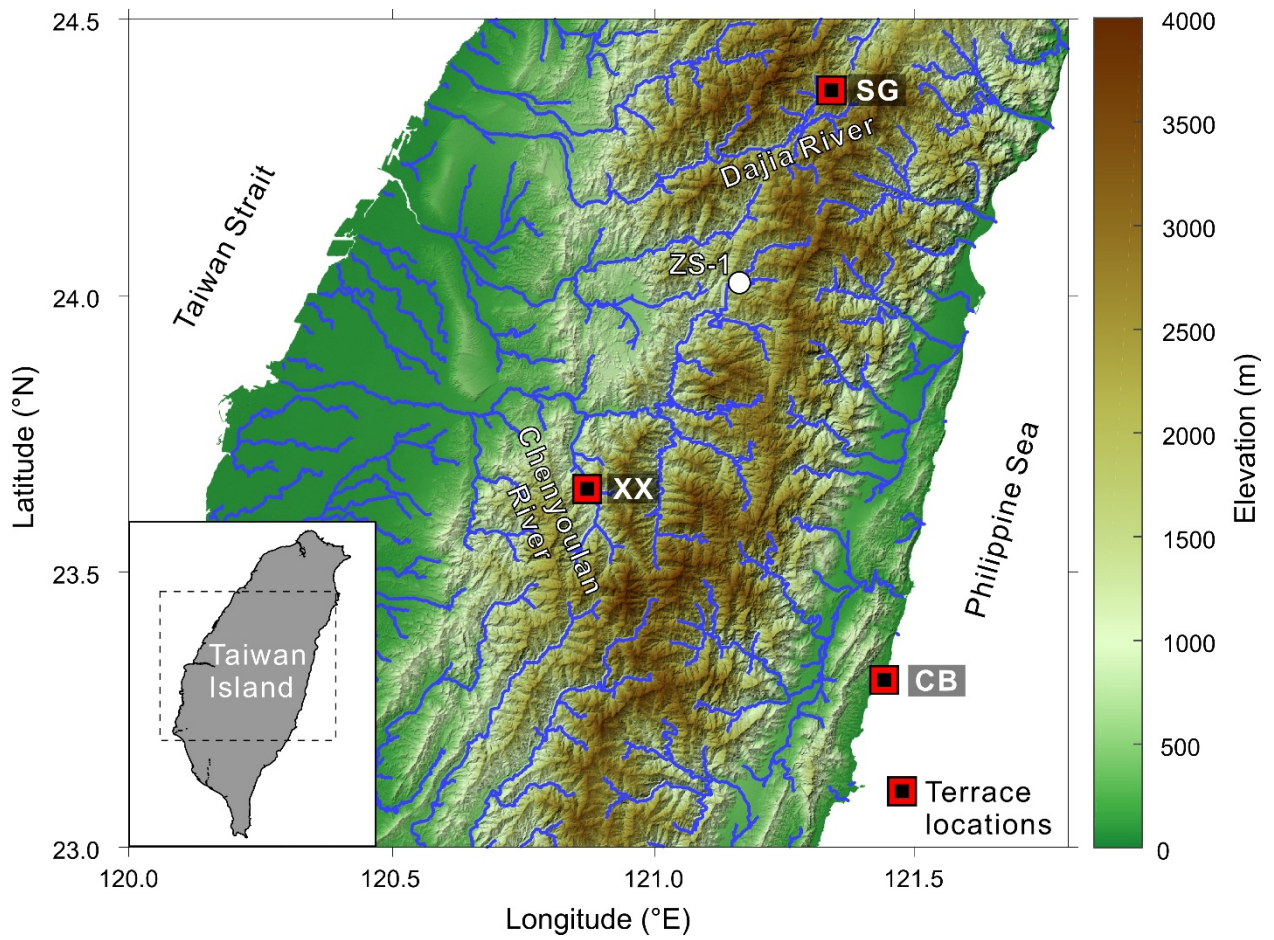


Fig. 1 Topographic map of Taiwan Island and terrace sampling locations. XX: Xinxiang terrace (Chenyulan River catchment); SG: Shengguang terrace (Dajia River catchment); CB: Changbin terrace (cored) located in the Coastal Range. ZS-1 is a modern river sediment in the headwaters of the Zhuoshui River (Deng et al., 2020b) close to terrace SG.

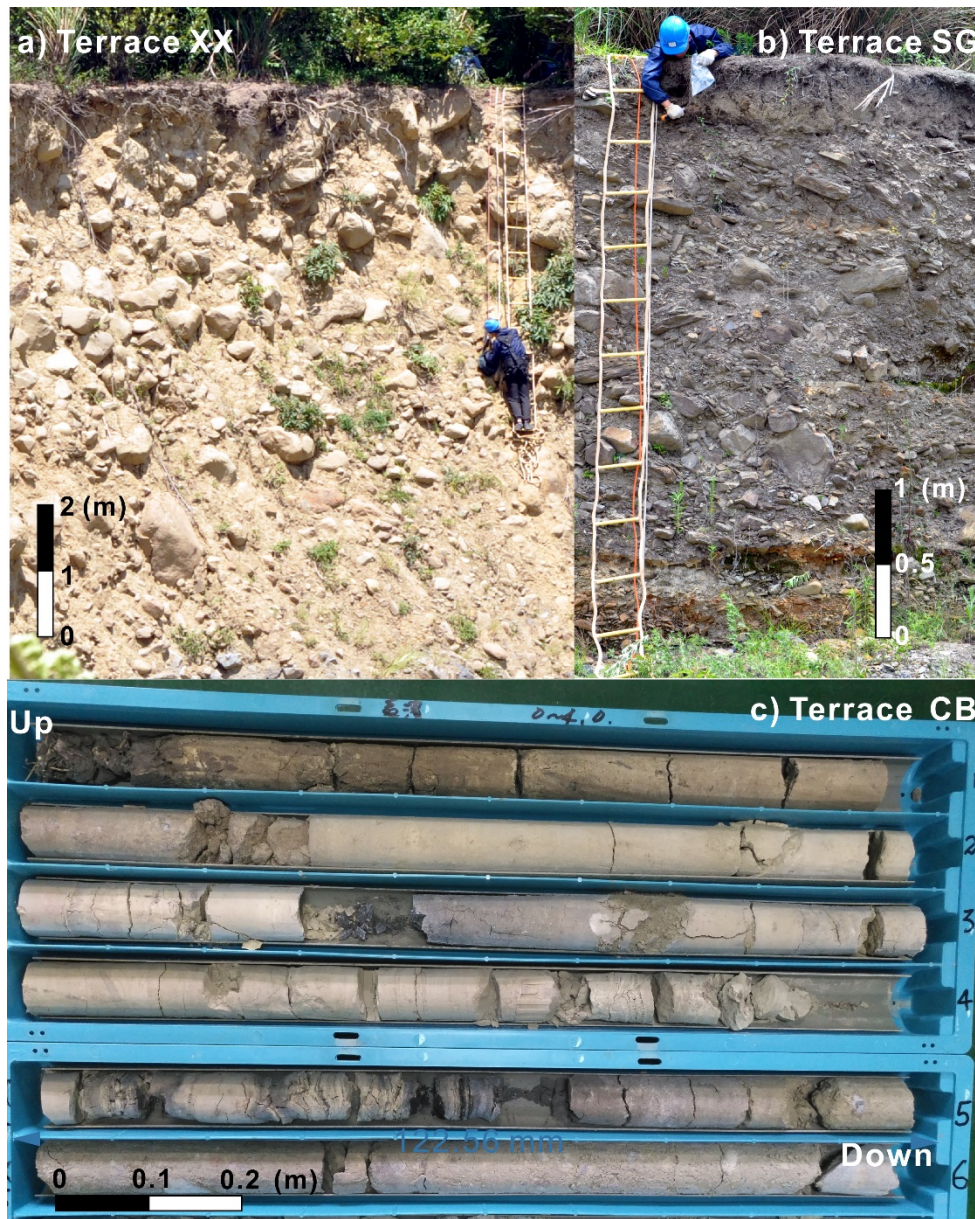


Fig. 2 Field photos for terraces XX (a), SG (b) and CB (c). Both images a) and b) are used for analyzing the areal percentage of unsampled boulders in each profile. No boulders were found in the sampled segment of a core drilled in terrace CB (c). Each segment in (c) is 1 m in length and 6 segments in total are shown.

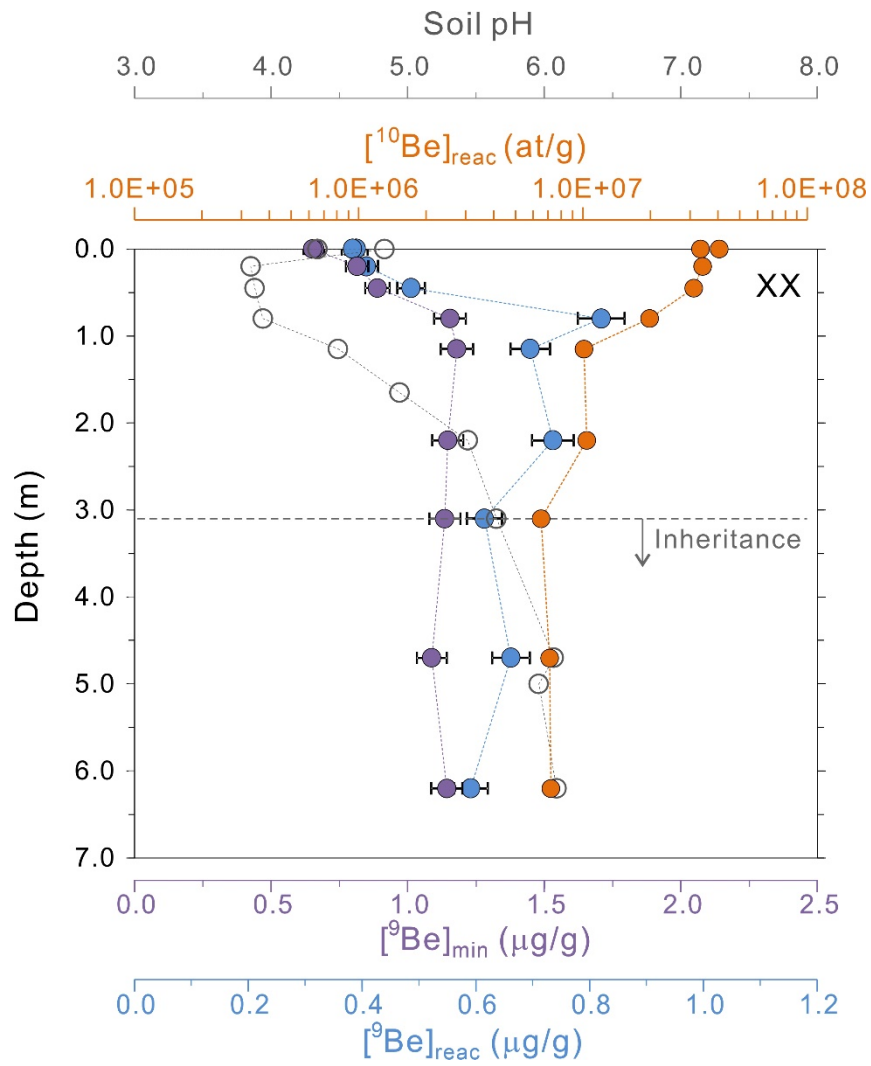


Fig. 3 Depth profiles of $[^{10}\text{Be}]_{\text{reac}}$, $[^9\text{Be}]_{\text{reac}}$, $[^9\text{Be}]_{\text{min}}$ and soil pH (in 0.01 M CaCl_2 , open symbols) in terrace XX (9.05 ± 0.35 ka). The axis of $[^{10}\text{Be}]_{\text{reac}}$ is in log scale.

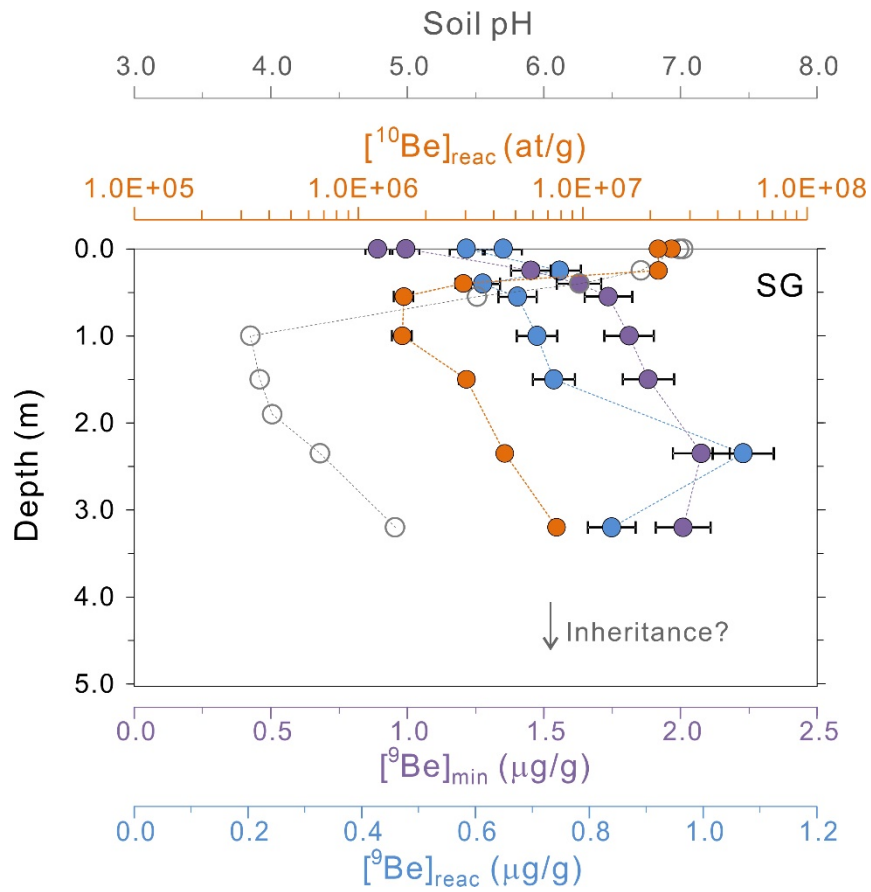


Fig. 4 Depth profiles of $[^{10}\text{Be}]_{\text{reac}}$, $[^9\text{Be}]_{\text{reac}}$, $[^9\text{Be}]_{\text{min}}$ and soil pH (in 0.01 M CaCl_2 , open symbols) in terrace SG (3.83 ± 0.36 ka). The axis of $[^{10}\text{Be}]_{\text{reac}}$ is in log scale.

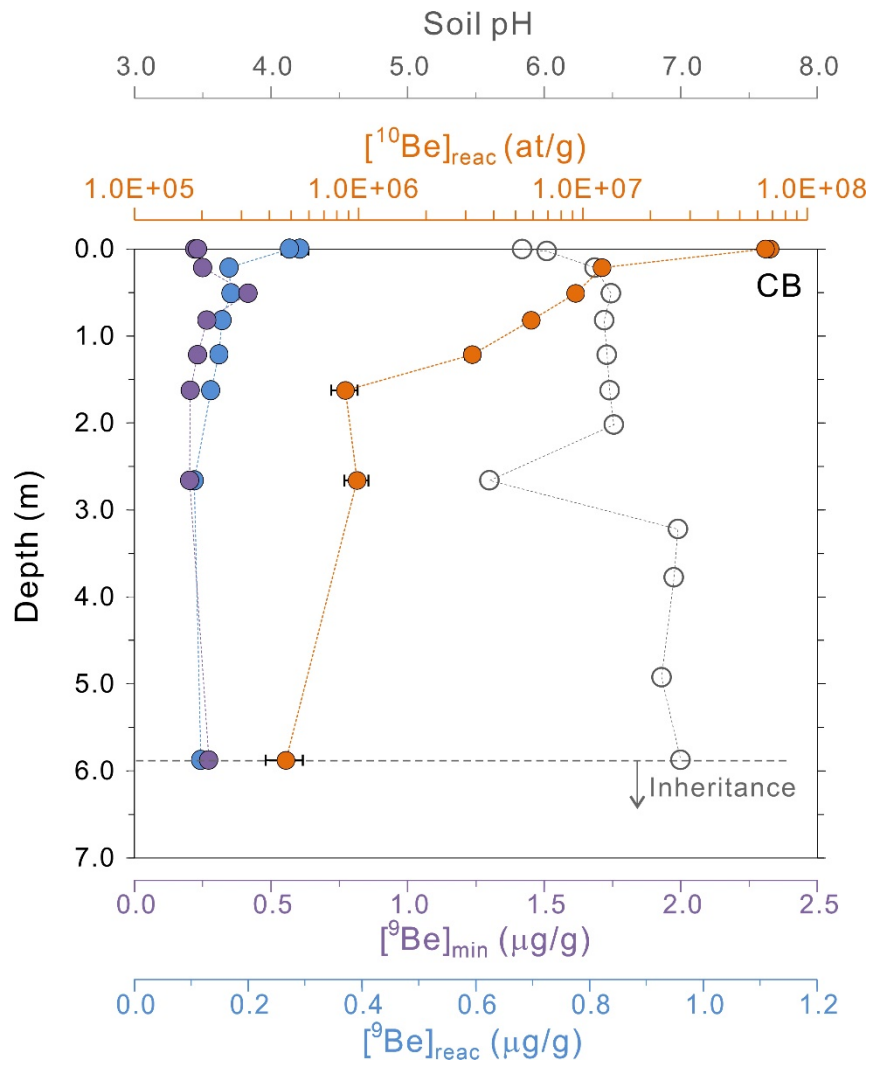


Fig. 5 Depth profiles of $[^{10}\text{Be}]_{\text{reac}}$, $[^9\text{Be}]_{\text{reac}}$, $[^9\text{Be}]_{\text{min}}$ and soil pH (in 0.01 M CaCl_2 , open symbols) in terrace CB (7.07 ± 0.89 ka). The axis of $[^{10}\text{Be}]_{\text{reac}}$ is in log scale.

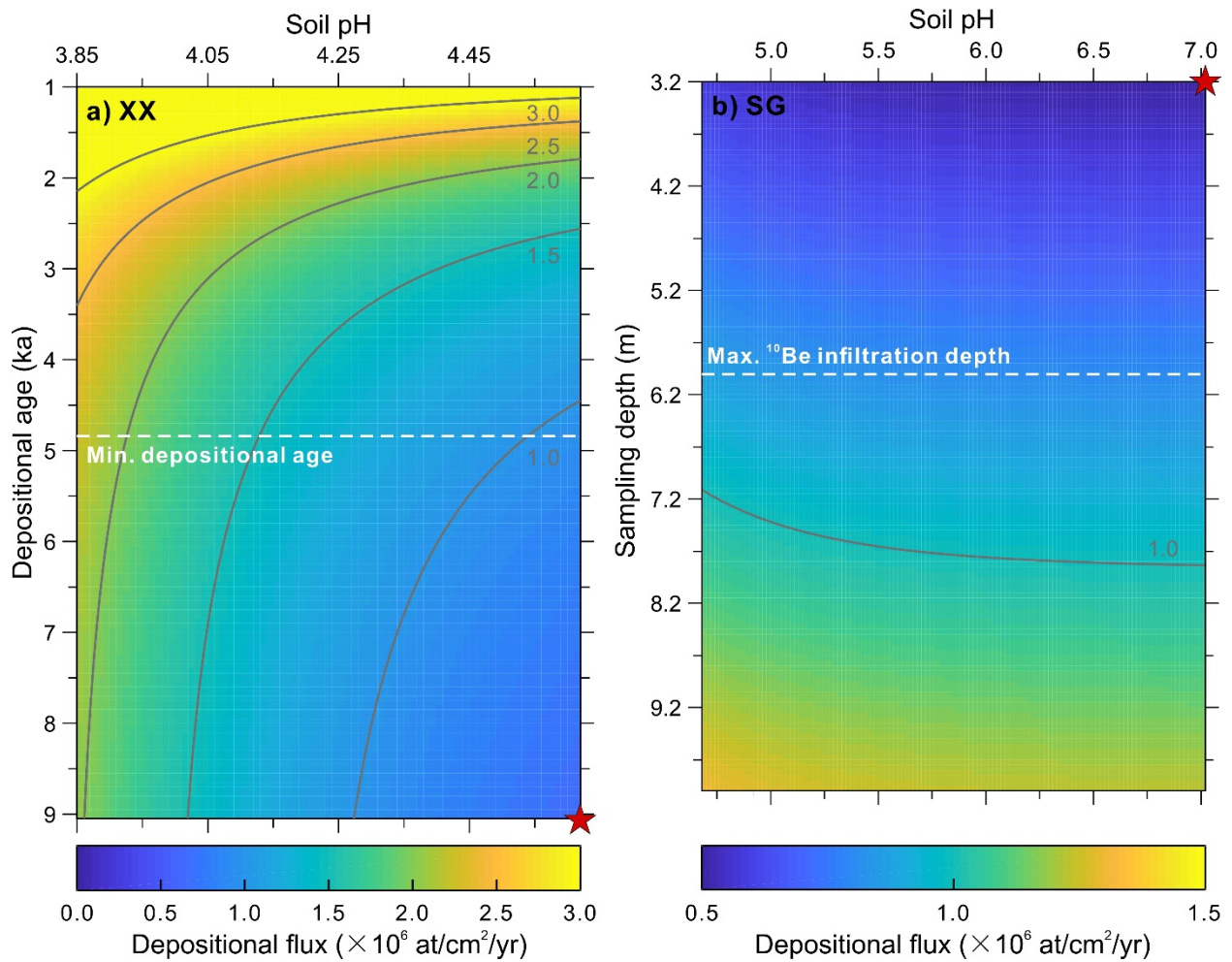


Fig. 6 Dependence of terrace-derived ^{10}Be depositional flux estimates (contour lines) on assumptions on soil pH as a proxy for ^{10}Be retentivity (X axis, panels a-b), depositional age (Y axis, panel a), and sampling depth (Y axis, panel b). a) Terrace XX, where incomplete Be retention and age overestimation likely introduce the largest bias; b) Terrace SG, where incomplete Be retention and incomplete sampling depth introduce bias. The depositional age of 9.05 ka in a) and the sampling depth of 3.2 m in b) indicate the original measured conditions. Details on setting the range of each axis, the minimum depositional age (a) and the maximum infiltration depth of ^{10}Be (b) are explained in Sections 5.2.1 and 5.2.2. Red star marks the lowest modelled ^{10}Be depositional flux within the given range of parameters in each figure.

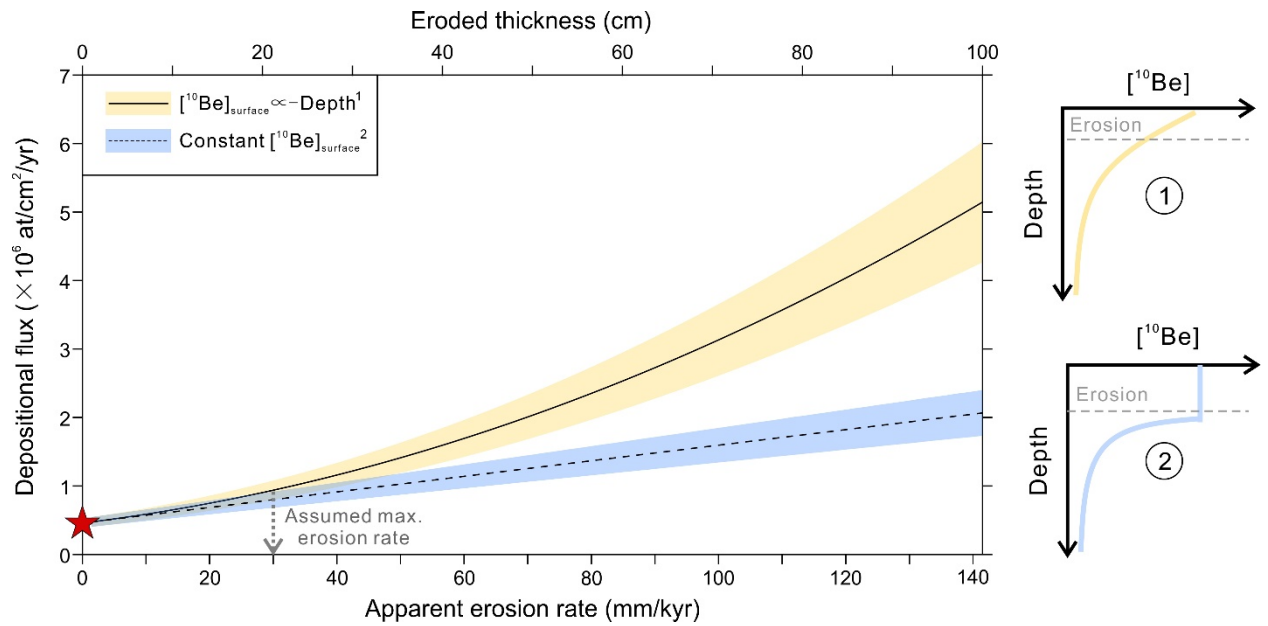


Fig. 7 Effect of surface erosion on ^{10}Be depositional flux estimates for terrace CB. The apparent erosion rate is calculated using eroded thickness divided by the terrace depositional age (7.07 ka). We evaluate two scenarios of ^{10}Be -depth patterns: ① linear decrease in ^{10}Be at the surface layer and ② constant ^{10}Be at the surface layer. The red star marks the calculated ^{10}Be depositional flux assuming zero surface erosion. The maximum erosion rate is assumed to be similar to that of Pakua terraces of western Taiwan (30 mm/kyr) estimated by *in situ* ^{10}Be depth profiles (Siame et al., 2012).

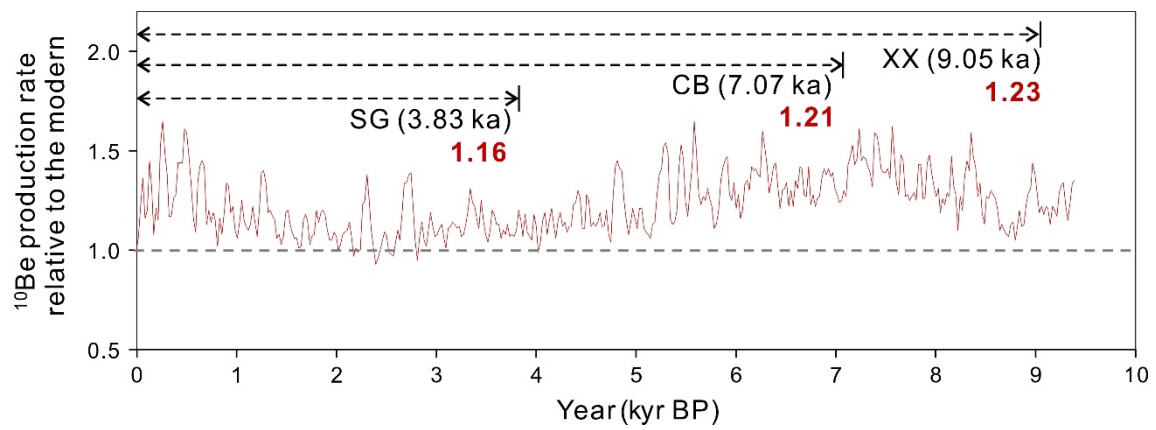


Fig. 8 The variations in global ^{10}Be production rates in the Holocene relative to the modern rate, modified from [Steinhilber et al., \(2012\)](#). The red numbers (1.16-1.23) indicate the time-averaged relative ^{10}Be production rate since deposition of each terrace. Note that the average relative ^{10}Be production rate in the Holocene is 1.23.

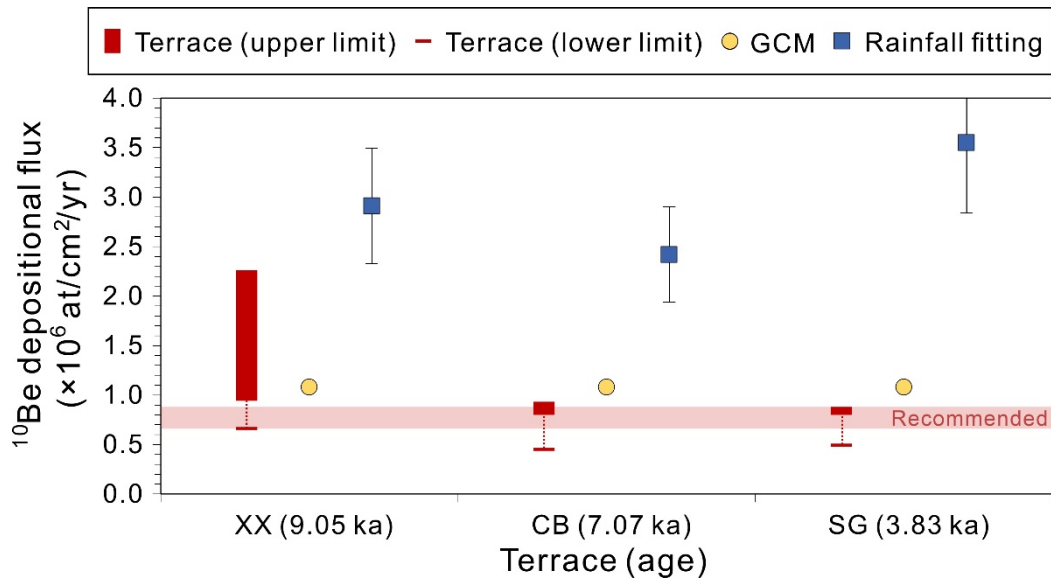


Fig. 9 Comparison between ^{10}Be depositional flux estimates from three independent approaches including terrace ^{10}Be inventories, GCM and rainfall-based fitting equation. The range of upper limit of terrace-derived fluxes is constrained by variable soil pH for terraces XX and SG (see details in Sections 5.2.1-5.2.2), and by two different scenarios of surface erosion for terrace CB (Section 5.2.3); the lower limit for each terrace is the same as the flux value marked by the red star in Fig. 6 or Fig. 7. The light red band is the overlapping range of flux estimates from three terraces ($0.66\text{--}0.88 \times 10^6$ at/cm²/yr). The uncertainty of GCM-derived fluxes (0.03×10^6 at/cm²/yr) is smaller than the symbol size (Heikkilä and von Blanckenburg, 2015). The uncertainty of fluxes from rainfall data fitting is 20% (Graly et al., 2011).